C-terminal-dependent control of EAAT2 signaling, corticostriatal synaptic glutamate clearance and spontaneous motor activity in mice with hypokinesia

Stefan Hirschberg*[1], Anton Dvorzhak*[1], Seyed M. A. Rasooli-Nejad[1], Svilen Angelov[1], Marieluise Kirchner[2,3], Philip Mertins[2,3], Gilla Lättig-Tünnemann[4,5], Christoph Harms[4,5], Dietmar Schmitz[6,7,8]and Rosemarie Grantyn[1,4,7,8]

*These authors equally contributed to the present work

1 Synaptic Dysfunction Lab, Neuroscience Research Center, Charité-Universitätsmedizin Berlin, Corporate member of Freie Universität Berlin, Humboldt-Universität zu Berlin, and Berlin Institute of Health, 10115, Berlin, Germany, stefan.hirschberg@charite.de, anton.dvorzhak@charite.de
2 Proteomics Platform, Max Delbrück Center for Molecular Medicine in the Helmholtz Association, 13125 Berlin, Germany
3 Berlin Institute of Health (BIH), 13125 Berlin, Germany
4 Department of Experimental Neurology, Charité-Universitätsmedizin Berlin, 10117 Berlin, Germany
5 Center for Stroke Research Berlin, Charité-Universitätsmedizin Berlin, 10117 Berlin, Germany
6 German Center for Neurodegenerative Diseases (DZNE), 10117 Berlin, Germany
7 Cluster of Excellence NeuroCure, 10117, Berlin, Germany
8 Einstein Center for Neurosciences Berlin, 10117, Berlin, Germany, rosemarie.grantyn@charite.de

For correspondence:
Prof. Dr. med. Rosemarie Grantyn
Neuroscience Research Center at
Charité-Universitätsmedizin Berlin
Robert-Koch-Platz 4
10115 Berlin, Germany
e-mail: rosemarie.grantyn@charite.de
Phone: +49-30-450528101
Fax: +49-30-450528952

ACKNOWLEDGEMENTS
Thanks are due to Profs. Arnd Baumann and Christoph Fahlke, Forschungszentrum Jülich for the EYFP EAAT2 S506X plasmid, Prof. Francisco Zafra, Universidad Autónoma de Madrid, for important information on the 4KR-edited EAAT2 isoform, Dr. K. Török, St. George's, University of London, and Dr. N. Helassa, University of Liverpool, for the $iGlu_u$ plasmid. Prof. Gudrun Ahnert-Hilger, Charité Universitätsmedizin Berlin, and Dr. Hannes Schmidt, Eberhard Karls Universität Tübingen, contributed numerous helpful suggestions. D. Betances and A. Schönherr provided excellent technical assistance. This work was supported by CHDI (A-12467), the German Research Foundation, under Germany's Excellence Strategy (Exc 2049 - 390688087) and intramural Charité Research Funds to R.G.

SUMMARY

Deficiency of the astrocytic excitatory amino acid transporter type 2 (EAAT2) and, consequently, inefficient glutamate clearance at corticostriatal synapses may contribute to the depression of self-initiated movements in Huntington's disease (HD). Here we report that the removal of the last 68 amino-acids in the C-terminal of EAAT2 increases the levels of native EAAT2 in striatal lysates and counteracts some of the HD-related changes in the interactor spectrum of mYFP-tagged EAAT2. Using the Q175 mouse model of HD, we explored the functional consequences of C-terminal modifications. It was found that astrocytic expression of EAAT2-S506X or -4KR alleviates the HD-related decrease in the incidence and velocity of exploratory movements. It also stimulates astrocytic glutamate uptake, increases the level of synaptic EAAT2 and improves glutamate clearance at single corticostriatal synapse. The experiments illuminate a link between the intracellular regulation of astrocytic glutamate transport in the striatum and symptoms of hypokinesia in HD mice.

KEYWORDS

Huntington's disease; EAAT2 interaction proteomics; Hypokinesia; Corticostriatal synaptic transmission; Glutamate clearance; Synaptic targeting of EAAT2

INTRODUCTION

HD is an autosomal dominant neurodegenerative disease. A trinucleotide (CAG) expansion of exon 1 in the mutant huntingtin gene (*mHTT*) causes abnormally long polyglutamine stretches in the already large huntingtin protein. *mHTT* is expressed not only in neurons but also in astrocytes (Faideau et al., 2010) where the loss of normal huntingtin function and additional effects of misfolded polyQ *mHTT* fragments can produce a large variety of functional alterations (Mrzljak and Munoz-Sanjuan, 2015;Tabrizi et al., 2019;Zeitler et al., 2019). HD patients suffer from progressive motor, cognitive and emotional disturbances (Tabrizi et al., 2013). A prominent motor symptom of advanced HD in humans and most rodent models of the disease is hypo-/bradykinesia (Hart et al., 2013;Horton et al., 2019;Berardelli et al., 1999), i.e. a reduced incidence and speed of self-induced movements. Chorea, i.e. the appearance of jerky uncontrolled spontaneous movements, is the predominant feature at earlier stages of HD (Tabrizi et al., 2013;Rosenblatt et al., 2003). Thorough quantification of the hypo- *vs.* hyperkinetic aspects of motor performance is important for the pharmacological management of the disease (Hart et al., 2013). In general, phenotype progression is less faithfully predicted by the scores of chorea as compared to those of hypo-/bradykinesia (Tabrizi et al., 2013;Rosenblatt et al., 2003).

According to the information available from extracellular recordings or imaging of neuronal activity in intact HD mice, motor symptoms may evolve as a consequence of disinhibition and abnormal synchronicity in the corticostriatal pathway (Miller et al., 2012;Burgold et al., 2019). Most studies point to functional uncoupling rather than enhanced glutamatergic input to the striatum (Plotkin and Surmeier, 2015;Reiner and Deng, 2018;Veldman and Yang, 2018). Moreover, there is a tendency for a down-regulation of vGlut1 immunofluorescence (Rothe et al., 2015), a decrease in the number of vGluT1+ terminals (Deng et al., 2013) and a reduction of synaptic glutamate release from individual corticostriatal terminals in mice with symptomatic HD (Dvorzhak et al., 2019). On the postsynaptic side, corticostriatal synaptic transmission might be affected by insufficient supply with brain-derived neurotrophic factor (Plotkin et al., 2014) or reduced signal transfer from distal dendrites (Carrillo-Reid et al., 2019). The duration of the NMDAR component of corticostriatal EPSCs was found to be prolonged (Dvorzhak et al., 2019), which might be due to a reduced glutamate clearance capacity of striatal astrocytes. Indeed, targeted expression of *mHTT* in astrocytes consistently impeded their glutamate uptake function (Bradford et al., 2009;Meunier et al., 2016;Faideau et al., 2010;Shin et al., 2005) and induced or exacerbated the motor symptoms of HD (Bradford et al., 2009;Meunier et al., 2016).

In the adult rodent striatum most of the glutamate transport is carried out by the excitatory amino acid transporter type 2 (EAAT2, gene name *Slc1a2*) (Vandenberg and Ryan, 2013;Danbolt, 2001;Beart and O'Shea, 2007). The EAAT2 protein is clustered at the sites of synaptic glutamate release (Danbolt, 2001) which ensures the rapid return of the extracellular glutamate concentration to very low resting levels (Bergles and Jahr, 1998). It is obvious that the impaired glutamate uptake, as observed in several mouse models of HD (Behrens et al., 2002;Bradford et al., 2009;Lievens et al., 2001;Meunier et al., 2016;Huang et al., 2010;Miller et al., 2008;Parsons et al., 2016;Faideau et al., 2010), must be a consequence of the *Htt* mutation, but the detailed mechanisms causing the proposed mismatch between glutamate release and clearance at corticostriatal synapses have remained unclear. At least four principal pathophysiological mechanisms have been considered in preceding studies: i) altered transporter-substrate interactions, ii) insufficient *Slc1a2* transcription, iii) deficient membrane targeting of EAAT2, and/or iv) exaggerated intracellular degradation of EAAT2. Heterologous expression studies with recombinant chimeric EAAT2 variants delineated the significance of functional compartments within the protein. It turned out that a region close to the distal end of the last transmembrane domain is relevant for the interaction with the transport substrate (Leinenweber et al., 2011), and affects the balance between cytoplasmic retention and membrane insertion (Kalandadze et

al., 2002;Underhill et al., 2015). Due to detailed studies from the Zafra lab, it is also known that ubiquitination of 4 C-terminal lysine sites (Gonzalez-Gonzalez et al., 2008) contributes to the internalization of the transporter from the plasma membrane. Finally, it was reported that sumoylated toxic C-terminal fragments may inhibit the *Slc1a2* transcription in the astrocyte nucleus (Gibb et al., 2007;Foran et al., 2011;Rosenblum et al., 2017). All these studies imply that EAAT2 binding partners at the C-terminal end participate in the regulation of glutamate uptake.

So far, a complete list of the intracellular binding partners of EAAT2 is not available. Accordingly, it is not known to what extent changes in glutamate uptake functions could be due to modifications in the EAAT2 interactome. Taking advantage of new genetic tools to explore structure-function relationships in more intact preparations, including mouse models of HD, we have obtained first results on the significance of C-terminal interactors for glutamate uptake, synaptic glutamate clearance and the symptoms of hypo-/bradykinesia. This information may help to delineate new targets for small molecule therapy in neurologic conditions associated with glutamate excitotoxicity.

RESULTS

Efficacy and specificity of viral vector expression in astrocytes

Fig. 1a provides an overview of the presently used viral vectors in search for modifiers of glial glutamate uptake in heterozygote Q175 mice (HET). Expression of the transgene was limited by the amount of injected particles (a single injection of $1.0*10^9$gc/striatum), the type of the viral serotype (PHP.eB), the selected promoter sequence (gfaABC1D) and the post-transcriptional regulatory elements (WPRE). All constructs were derived from human EAAT2 variants, with the understanding that there is a close similarity in the sequence between the human and mouse *Slc1a2* homologues (Kirschner et al., 1994). At the same time it is obvious that we will only compare between the effects of control versus test vectors, the reference group being "HET-CTRL" (see Supplemental Tab. 1).

The first EAAT2 variant ("EAAT2-S506X") has a truncation at S506 resulting in the removal of the last 68 amino acids. The second one ("EAAT2-4KR") has four point mutations at the C-terminal end. The third construct ("EAAT2") contains the full-length expression cassette. For detection purposes, the N-terminal of the transporter sequence was fused to mYFP or mRuby3. Reporter constructs without EAAT2 served as controls ("CTRL") and were, as all the other constructs, bilaterally injected in WT and HET striatum.

Immunostained fixed sections were used to quantify the number of transgene-expressing cells in the dorsal striatum (Fig. 1b-d). Cell counts and functional imaging were performed at a mediolateral distance of 2-2.5 mm within the boxed area. Fig. 1e, f illustrates that the area of evaluation was always well within the extensively labeled zone. The latter covered about 40% of the striatal volume. An "effective transduction rate" (ETR) was determined in 4 mice, each contributing about 10 viewfields. Co-localization of the fluorescent tag with a suitable cell-specific marker rendered the following ETR values: S100β+ cells (astrocytes) - 65.9 ± 2.47%, NeuN+ cells (neurons) - 2.76 ± 0.44%, Iba1+ cells (microglia) - 1.64 ± 0.85%. There also was some labeling in the overlaying cortex and a small degree of unintended transgene expression in neurons and microglial cells. Among the population of mRuby+ cells in the dorsal striatum (boxed area in Fig. 1e), 90.8% were astrocytes, 8.3% - neurons and 1.6% - microglial cells. These results were considered appropriate to compare the effects of TEST as opposed to CTRL vectors in HET and to find out whether TEST-induced changes approximate the condition of WT-CTRL.

Motor phenotype of injected Q175 HET and effects of the C-terminal-truncated variant of EAAT2

In Q175 HET older than 1 year motor performance has not yet been characterized in much detail. Here we present new results from rapid assessment and detailed analysis of self-initiated motor activity before and after viral treatment. The mice underwent two video-recorded tests: i) the open field test, OFT (Menalled et al., 2012;Rothe et al., 2015) and ii) the step-over latency test, SOLT (Dvorzhak et al., 2019). The latter was developed in our lab and could be regarded as a direct indicator of the time needed to initiate exploration in the open field. The present data from injected mice is validated by a larger number of observations from noninjected mice (compare Fig. 2d and Supplemental Fig. 1c). Step-over latencies longer than 300 ms were only seen in <5% of the WT sample, whereas 25% tests in the HET group produced values >300 ms (Supplemental Fig. 1d).

As one of the commonly used OFT indicators, the total path travelled was decreased in Q175 HET (Fig. 2a, c). Of particular interest was a characterization of the transition from rest to running, for instance by counting the number of starts (Fig. 2a, green spots, and Fig. 2b). The quantification shows that the incidence of starts was indeed lower in HD (Fig. 2d). Moreover, the step-over latency (Fig. 2e) exhibited a significant negative correlation with the incidence of starts from rest (Fig. 2f). Possibly related to these findings is the larger maximal to mean radius of the resting area, i.e. the extension of the resting area until a new movement starts (Fig. 2b, g). For the definition of resting *vs.* running episodes see Supplemental Tab. 3.

We also considered the possibility that HD differentially affects movement velocity during running and resting, since striatal gamma oscillation, a phenotypic marker of symptomatic HD, only occurs at rest (Rothe et al., 2015). This might be the case, but both indicators exhibited a similar response to treatment (Fig. 2h, i). Other parameters derived from the OFT were unchanged by viral treatment, such as the relative time spent in the open field center or in the resting state (Fig. 2j, k). One may argue that the latter indicators are not representative for exploratory motor activity.

In the following the term "hypokinesia" will apply to HD mice with i) increased step-over latency, ii) reduced incidence of starts from rest, iii) increased maximal to mean deviations from the center point, at rest, iv-v) decreased movement velocity during running and resting, and vi) a smaller total distance travelled. Accordingly, the term "recovery from hypokinesia" would refer to a significant change towards the respective WT values. But would such a recovery be possible at all? And, if so, under what conditions? The answer seems to be: YES. Under appropriate conditions, i.e. with a suitable EAAT2 vector construct (EAAT2-S506X), a spatial restriction of the vector access (single striatal microinjections of PHP.eB) and an astrocyte-specific promoter (gfaABC1D) it was indeed possible to obtain recovery with respect to all 6 indicators of hypokinesia. Some data reflecting less successful attempts will be mentioned in the Supplemental Text, but it is out of scope to analyse the reasons of failure in detail.

Together, the experiments suggest i) that the state of striatal astrocytes is relevant for the incidence and speed of exploratory movements and ii) suppression of adverse signals via the EAAT2 C-terminal might be an effective means to restore glutamate uptake.

Rescue of astrocytic glutamate uptake following the expression of C-terminal-modified EAAT2 in the striatum

To gain further information on the functional consequences of C-terminal modifications in HD, imaging experiments were performed in striatal slices loaded with the Na^+ indicator SBFI-AM. The major part of the response to bath-applied L-aspartate was blocked by the high-affinity glutamate transporter inhibitor TFB-TBOA (Fig. 3a), and this TFB-TBOA-sensitive component of the Na^+ elevation was quantified in WT-CTRL, HET-CTRL and two HET-TEST groups with C-terminal-

modified EAAT2. The records of averaged responses (Fig. 3b) visualize the differences between WT and HET and the similarity of responses obtained in the WT-CTRL, EAAT2-S506X and EAAT2-4KR groups. Multilevel (nested) ANOVA confirmed a significant rescue of the L-aspartate induced sodium response in astrocytes transduced with EAAT2-S506X and EAAT2-4KR (Fig. 3c and Supplemental Tab. 1). Our SBFI-loading protocol was adjusted to preferentially label astrocytes (Dvorzhak et al., 2016). This offered an opportunity to determine, in the same viewfield, the glutamate uptake of transduced versus non-transduced astrocytes (Fig. 3d, e). In the case of HET-EAAT2-S506X, there was a significant difference between the transduced and not-transduced astrocytes (Fig. 3f).

These results show that the expression of the C-terminal-modified EAAT2 variants indeed counteracts the HD-induced depression of glutamate uptake. Substitution of the 4 lysine sites is almost as effective as the C-terminal truncation.

Mice with systemic application of EAAT2-S506X failed to outperform mice with intrastriatal injections

See Supplemental Text and Supplemental Fig. 2.

Transduction with the full-length EAAT2 vector failed to abolish the symptoms of hypokinesia and to rescue glutamate uptake

See Supplemental Text and Supplemental Fig. 3.

Effects of EAAT2-S506X on native EAAT2 levels

The reduced glutamate uptake activity in HD has often been associated with a lower level of the EAAT2 protein in the striatum. To the best of our knowledge, this information is not available for Q175 mice aged 15 months and older. The current experiments fill that gap of knowledge and provide further information on the possible effects of EAAT2-S506X expression on the levels of native EAAT2, i.e. the intrinsic transporter protein without tag. Striatal lysates from three animal groups were prepared for Western blot analysis (Fig. 4a, b). In non-injected WT mice, native EAAT2 immunoreactivity (IR) is represented with a major band at about 62 kD (***). WT mice injected with a full-length EAAT2 fused to an N-terminal mYFP show an additional band at about 89 kD (**). As expected, this band reacts with antibody (Ab) against mYFP and EAAT2 (Fig. c, d). In the EAAT2-S506X group the respective band is only detectable with mYFP-Ab but not EAAT2-Ab, because all EAAT2-Abs that performed well, in our hands, were generated to a synthetic C-terminal peptide which is absent in in the C-terminal-truncated EAAT2-S506X construct. Accordingly, the EAAT2 band is seen with mYFP-Abs but at lower molecular weight (compare boxed area in Fig. 4d, e). This opens an interesting opportunity to quantify effects on the native murine EAAT2 (i.e. * + ***). It can be seen (Fig. 4f) that expression of the full-length EAAT2 construct did not abolish the HD-related difference in the total EAAT2 protein, while EAAT2-S506X resulted in EAAT2 IR elevation, even though in this case the contribution of mYFP-EAAT2 is not included. Only the * + *** bands, i.e. the intrinsic EAAT2, could contribute to the measured EAAT2 IR. Please note that all three test groups exhibited a similar level of IR to mYFP (Fig. 4g).

These findings are consistent with the idea that the beneficial effects of the C-terminal-modified EAAT2 constructs on glutamate uptake do not solely reflect EAAT2 substitution. One may consider the additional hypothesis that EAAT2-S506X increases the availability of native EAAT2.

Mass-spectrometry-based proteomics revealed HD-related changes in the interactor spectrum of full-length EAAT2 and effects of EAAT2-S506X

Using mYFP as "bait" we precipitated full-length and truncated EAAT2 proteins with magnetic beads linked to an anti-YFP "nanobody" (Fig. 5a). Fig. 5b, c shows that the immunoprecipitate contained a sufficient and similar amount of mYFP in the materials obtained from the 3 animal groups selected for in-depth analysis of the EAAT2 interactors.

The experiments were designed to compare i) in HET *vs.* WT, the EAAT2 interactors of full-length EAAT2 and ii) in HET only, the EAAT2 interactors of truncated *vs*. full-length EAAT2. Each experiment was performed in at least 4 mice, with 2 repetitions per animal. Fig. 5d lists 20 significant EAAT2 interactors selected according to the size/direction of the HD-related differences. The empty bars/black asterisks reflect the differences between the WT-EAAT2 and HET-EAAT2 groups, i.e. the effects of HD as such. The filled bars/green asterisks show the respective log2 differences between the HET-EAAT2-S506X and the HET-EAAT2 groups. This data reflects the impact of C-terminal truncation and may include rescue effects. Please note that the experiments cannot show what actually happens to the native murine EAAT2 protein devoid of mYFP, but rather provide a first glimpse at the normal and pathological EAAT2 binding partners that may influence the glutamate uptake function in astrocytes. It can, for instance, be seen that the interaction with dystrophin (gene name *Dmd*) is decreased in HD and partially restored in HET treated with EAAT2-S506X. Most interesting, HD is also associated with a substantial up-regulation of potential EAAT2 interactors, an example being UBA2, the ubiquitin-like 1-activating enzyme E1B, also known as SUMO-activating enzyme subunit 2 with the gene name *Uba2*. This interaction is strongly reeduced by the truncation of the C-terminus in the HET-S506X group. Other highly abundant and significant interactors of EAAT2 were not affected by HD (Fig. 5e).

To summarize, our proteomics data are consistent with the hypothesis that: 1) the EAAT2 interactome is influenced by HD, 2) some of the HD-related changes are reversible and 3) expression of C-terminal-truncated EAAT2 may block abnormal sumoylation and promote more physiological protein interaction patterns.

Rescue of normal synaptic glutamate clearance after striatal expression of EAAT2-S506X

At a cellular level, effects of EAAT2-S506X can reveal themselves at a large number of sites throughout the mouse brain. However, given the importance of the corticostriatal pathway for the initiation of motor activity and the involvement of astrocytic glutamate transport in the clearance of synaptically released glutamate, it was decided to quantify synaptic glutamate uptake in EAAT2-S506X mice. In the present experiments, individual synaptic glutamate transients were resolved by using CaMKII-driven expression of the genetically encoded "ultrafast" glutamate indicator $iGlu_u$ from the Török lab (Helassa et al., 2018). As the striatum is devoid of glutamatergic neurons, $iGlu_u$ fluorescence of single corticostriatal presynaptic varicosities could well be resolved even under condition of blocked action potential generation. This helps the application of standardized tests at the synapses of choice (Dvorzhak et al., 2019). Two types of corticostriatal synapses were identified according to the size of $iGlu_u$-positive varicosities at rest and their response dynamics during repetitive activation. Large (>0.63 µm) fluorescent terminals with paired pulse facilitation (PPF) were assumed to belong to the group of PT-type afferents formed by the layer V pyramidal neurons of the motor cortex (Reiner and Deng, 2018;Dvorzhak et al., 2019). The specimen records selected for Fig. 6a illustrate the differential extension of the glutamate elevation in the perisynaptic space. It can be seen that the parameter "Spread" (see Methods for definition) was sensitive to treatment with EAAT2-S506X (Fig. 6a, c).

More information could be derived from the reconstruction of the time-dependent changes of the mean intensity values from all suprathreshold pixels monitored at the given synapse of interest. Fig. 6b

shows the $iGlu_u$ intensity changes (as ΔF/F%) induced by a short biphasic electrical stimulus applied via a glass pipette directly to the synapse. The traces could be used to extract two important indicators: "Peak amplitude" (short red horizontal line) and the time constant of decay ("TauD", see values next to the red monoexponential fitting curve). Similar traces were constructed from single pixels. The transients derived from the pixel with the highest fluorescence increase reflect the release and clearance of glutamate in the immediate vicinity of the "active zone", i. e. the site of vesicle exocytosis. The respective values are summarized in Supplemental Tab. 1.

Fig. 6c-e shows the results based on the quantification of the mean suprathreshold pixel values. It can be seen that Spread and TauD, but not Peak amplitude were affected by the expression of EAAT2-S506X. It is assumed that Spread and TauD are more closely related to the astrocytic glutamate uptake while Peak amplitude reflects, first of all, the amount of released glutamate. TauD is particularly useful for the identification of dysfunctional synapses in HD, as TauD values larger than 15 ms have never been observed in WT (Dvorzhak et al., 2019). In contrast, ~40% of PT synapses tested in HET at an age of ~16 months exhibited TauD values >15 ms. Now we show that in HET treated with EAAT2-S506X synapses with prolonged decay were entirely absent (Fig. 6f). It should be pointed out that the present single synapse data has exclusively been collected from terminals located on the territory of transduced astrocytes. The arrowhead of Fig. 6g points to a bright varicosity on the background of the red fluorescent area generated by the dendritic field of one Ruby-expressing astrocyte. These spatial interrelations are relevant for understanding the mechanisms of synaptic modulation by astrocytic transporters or gliotransmitters.

Thus, the results presented in Fig. 6 and Supplemental Tab. 1 could help to clarify two issues. They support the astrocytic origin of HD-related pathology in the corticostriatal pathway and demonstrate the return towards WT levels of synaptic glutamate clearance after treatment with the truncated EAAT2.

Striatal expression of EAAT2-S506X or EAAT2-4KR increases the abundance of EAAT2 protein at single corticostriatal synapses

Next it was asked whether effects of EAAT2-S506X (or EAAT2-4KR) could be discerned even in EAAT2 immunostained sections. Please note that the used Ab only works against EAAT2 with intact C-terminal. This was a necessity (alternative antibodies to other domains failed to give satisfying results in synaptic staining), but also an interesting prove-of-principle opportunity to verify the conclusions from Fig. 4d, e, were EAAT2-S506X expression increased the level of native EAAT2. Fig. 7 shows the results from four simultaneously processed test groups, each consisting of two CAG-, age- and body weight- matched animals: "WT-CTRL", "HET-CTRL", "HET-EAAT2-S506X" and "HET-EAAT2-4KR". The selected immunostained sections (Fig. 7a) already illustrate a noticeable shift towards lower EAAT2 intensity levels in HET as compared to WT mice. Fig. 7b illustrates the respective single synapse immunofluorescence (IF) in small ROIs with only one vGluT1-positive spot, i.e. one corticostriatal presynaptic terminal. The EAAT2-positive pixels co-localize with mRuby3, i.e. they belong to an astrocyte process. The graph of Fig. 7c and the Supplemental Tab. 1 show the results of statistical evaluation of the EAAT2-immunofluorescent clusters within the analyzed ROIs. Both the HET-EAAT2-S506X and the HET-EAAT2-4KR groups differed from the HET-CTRL group which points to elevation of the synaptic EAAT2 protein abundance to almost WT level.

In combination with the results of vital single synapse glutamate imaging (Fig. 6) the IR data can be considered as another useful piece of evidence underlining the importance of astrocytic EAAT2 at tripartite corticostriatal synapses. In addition, the results identify the expression of C-terminal-modified EAAT2 as a possible means to elevate the level of perisynaptic EAAT2.

Effect of striatal S506X injections on neuronal excitability

In the Supplemental text, we present further results illustrating the influence of HD on neuronal excitability. But the effects of EAAT2-S506X remained below the significance level required with nested ANOVA (Supplemental Fig. 4).

DISCUSSION

The results underscore the importance of C-terminal-dependent EAAT2 binding partners and support the hypothesis that HD-related deficits in motor activity, astrocytic glutamate uptake and synaptic glutamate clearance can be alleviated by the expression of a C-terminal-modified EAAT2 transgene.

What is the molecular basis of failing glutamate uptake in HD?

Several mRNA transcripts have been identified to produce EAAT2 splice variants, with some degree of cellular and regional specificity and differential localization within one and the same astroglial cell (Sullivan et al., 2004). In rodents C-terminal-related differences exist between the two isoforms GLT1a and GLT1b (Underhill et al., 2015). The former is more mobile at synaptic sites (Al Awabdh et al., 2016). Experimental immobilization of EAAT2 has been shown to prolong synaptic currents (Murphy-Royal et al., 2015). Given that the duration of the glutamate transport cycle (~ 12 ms at Schaffer collateral synapses (Bergles and Jahr, 1998)) is relatively long in comparison with the glutamate receptor binding, it was hypothesized that lateral movement of the substrate-transporter complex and a rapid membrane turnover to replenish fresh unbound transporter molecules are necessary for effective glutamate buffering at synaptic sites. How the degradation/replenishment at the site of glutamate release works is not yet clear. But to ensure the high abundance of transporter molecules at synaptic sites (Lehre and Danbolt, 1998) the turnover of the transporter from the cytoplasm into the membrane should also be high.

Experiments in HEK293 cells showed that internalization of EAAT2 is promoted by its association with the adaptor protein beta-arrestin and the ubiquitin ligase Nedd4-2 (Ibanez et al., 2016). In the absence of more detailed knowledge, these experiments hint potential sites of EAAT2 regulation as it was shown that Nedd4-2 knockdown decreased glutamate transporter ubiquitination, promoted glutamate uptake and increased glutamate transporter expression *in vitro* and in the MPTP mouse model of parkinsonism (Zhang et al., 2017). Our present experiments in symptomatic Q175 HET are, to the best of our knowledge, the first attempt to characterize an HD phenotype in the EAAT2 interactome by using immunoprecipitation of mYFP-tagged native and C-terminal-truncated EAAT2 as "bait". Our focus was on the alterations produced by the disease, on one side, and the C-terminal truncation of EAAT2, on the other side. It was quite obvious that the disease resulted in major changes in the abundance of full-length EAAT2 binding partners, with the disappearance of normally existing, potentially necessary interactors, such as dystrophin, and the appearance of new, potentially pathological interactors, such as UBA2.

Dystrophin is quite plentiful in astrocytes, especially at the endfeet, and it has been shown that dystrophin-glycoprotein complexes provide a link between laminin and the cytoskeleton (Sato et al., 2018) thereby contributing to the stabilization of aquaporin4 and Kir4.1 in particular subregions of the astrocyte plasma membrane (Enger et al., 2012). A function of dystrophin at glutamatergic corticostriatal synapses has not yet been explored, but there is evidence for a role of a dystrophin-associated protein complex in the pathogenesis of parkinsonian symptoms (Spuler et al., 2010).

UBA2 and SAE1 form a heterodimer that functions as a SUMO-activating enzyme. Sumoylation - the covalent attachment of SUMO1 to lysine residues - is a posttranslational modification process with

relevance to HD (Steffan et al., 2004). Interestingly, non-sumoylated EAAT2 resides in the plasma membrane while the product of SUMO fusion with EAAT2 tends to form aggregates in the cytoplasm (Foran et al., 2011). In the present study, when comparing the UBA2 levels precipitated by mYFP-EAAT2 or mYFP-EAAT2-S506X from HET animals, it was apparent that the loss of C-terminal interaction motives largely prevented the interaction between EAAT2 and UBA2.

In cultured astrocytes, a proteolytically released C-terminal fragment of EAAT2 modified by SUMO1 was also found in the nucleus, with inhibitory effects on EAAT2 transcription (Gibb et al., 2007;Foran et al., 2011). The relevance of this EAAT2-derived signaling mechanism was demonstrated *in vivo*, in a mutant SOD1 mouse model of amyotrophic lateral sclerosis (ALS), where knock-in of a modified *Slc1a2* isoform with a defective caspase-3 cleavage site prolonged the life span of mice afflicted by the disease (Rosenblum et al., 2017).

As for the plasma membrane localization of EAAT2, it should be noted that there is a basal constitutive internalization of the transporter, with a critical role of the lysines 497, 517, 526, 550, 558, 570, and 573 at the EAAT2 C-terminal (Martinez-Villarreal et al., 2012;Gonzalez-Gonzalez et al., 2008). It is interesting that in the present SBFI imaging experiments a selective lysine-to-arginine exchange in the C-terminal of the EAAT2 protein proved to be almost as effective as the C-terminal truncation suggesting a critical role for C-terminal lysine-mediated interactions such as SUMOylation and ubiquitination in the regulation of glutamate uptake.

In the context of the above literature on constitutive internalization of EAAT2 and the toxic effects of sumoylated C-terminal EAAT2 cleavage products, it is tempting to propose that an astrocyte expressing *mHTT* presents with largely altered conditions for both transcriptional control <u>and</u> protein sorting, which perhaps explains why in Q175 HET an mere stimulation of full-length EAAT2 failed to eliminate the deficits in the motor performance and glutamate uptake seen in HET CTRL group. Of course, much more work is needed to fully unravel the molecular determinants of EAAT2 function in the striatum and other regions of the brain.

Which cellular markers report failure or rescue of glutamate clearance?

SBFI imaging of substrate-induced transport activity has provided useful information on the EAAT2 deficiency of single astrocytes in the striatum of HD mice (Dvorzhak et al., 2016). In Q175 HET, cellular signs of HD were consistently found at an age of >1 year, when the mice displayed the described alterations of exploratory behavior. Of primary interest is, of course, the measurement of glutamate uptake. Here we have quantified the glutamate-uptake-related sodium signals obtained from a small ROI within the territory of only one astrocyte. In comparison with tissue glutamate uptake, this indicator should be less affected by other HD-induced alterations, such as changes in the size and density of astroglia in the striatum. After correction for inter-animal variance and demonstration of the HD phenotype in Q175 HET, the experiments with C-terminal-modified PHP.eB-gfaABC1D-EAAT2 vectors provide evidence for rescue. This adds an essential piece of evidence to support the idea that the HD-related hypokinesia and the deficits in synaptic glutamate clearance reflect, first of all, changes in: i) the *mHtt*-expressing astrocytes, ii) the EAAT2/GLT-1 regulation and iii) signals via the EAAT2-C-terminal, as opposed to changes in other cell types, transporter proteins or EAAT2 domains.

Experiments on the role of EAAT2 in corticostriatal synapses have become feasible since the genetically encoded glutamate sensor $iGlu_u$ was introduced into the field of synaptic transmission (Helassa et al., 2018). Experiments in our lab showed that application of TFB-TBOA, an unspecific blocker of glutamate transport, prolonged the duration of synaptically induced glutamate transients while treatment with ceftriaxone (CEF), a wide-range stimulator of NF-κB-dependent transcription

activators (Lee et al., 2008;Ghosh et al., 2016) was followed by a shortening of NMDAR-mediated corticostriatal EPSCs (Dvorzhak et al., 2019). Given the significance of the corticostriatal pathway in the initiation of self-induced movements and the high degree of compartmentalization of cortical input to individual SPNs, it was important to introduce a quantitative measure for the evaluation of glutamate release and clearance at the level of individual corticostriatal synapses. The TauD values obtained from fitting monoexponential functions to the decay of the glutamate transients were found to be well suited for the identification of potentially dysfunctional synapses. Additional information on the HD-induced alterations and the rescue effects achieved with C-terminal-modified EAAT2 was obtained by estimating the spread of synaptically released glutamate and the level of EAAT2 IR at single corticostriatal terminals (Supplemental Tab. 1).

This is the first time that such rigorous bidirectional (WT *vs.* HET and HET *vs.* HET-TEST) structure-function analysis has been carried out in aged HD mice. But there still are questions to be addressed by further experiments. First of all, one has to consider that the relationships between the perisynaptic astrocyte processes (PAPs) and the presynaptic glutamate release sites might not been uniform. A comparison between synapses established by vGluT1+ (i.e. corticostriatal) as opposed to vGluT2+ (i.e. thalamostriatal) terminals suggests that there might be circuit-specialized astrocyte-synapse interactions (Chai et al., 2017). A respective proximity assay in R6/2 mice from the Khakh lab (Octeau et al., 2018) showed that the incidence of very close terminal-astrocyte proximity decreased due to HD at corticostriatal synapses, but increased in thalamostriatal synapses. The proximity between PAPs and presynaptic glutamate releasing sites has been implicated in the mechanism regulating synapse plasticity by changing the conditions for glutamate buffering (for instance (Murphy-Royal et al., 2015)). Thus, IT-type synapses (i.e. bilateral afferents from the layer 2/3 pyramidal afferents) and thalamocortical synapses may show no or different changes in HD. An examination of these functionally very important components of motor control (Morita, 2014) will still be needed.

Is region- and cell-type-restricted expression of artificial EAAT2 variants a useful approach to study disease-related pathology?

HD is a disease that can be diagnosed much before the onset of motor symptoms. Great efforts are therefore being made to reduce the expression of *mHTT* inside and outside the central nervous system (Mrzljak and Munoz-Sanjuan, 2015;Tabrizi et al., 2019). *mHTT*-lowering therapies have reached an advanced stage of preclinical testing or even entered the phase of first clinical trials (Mullard, 2019). In animal models of HD, the most effective approaches include the use of self-inactivating KamiCas9 system for editing the huntingtin gene (Merienne et al., 2017), injection of *mHTT* transcription-targeting viral vectors (Zeitler et al., 2019) and application of siRNAs, shRNAs or miRNAs for the reduction of *mHTT* mRNA and protein level (see (Kaemmerer and Grondin, 2019) for review).

It is obvious that gene therapy is becoming more problematic at symptomatic stages of the disease. In HD, as well as other neurodegenerative disorders, late-stage pathology would always include numerous compensatory mechanisms which would make it increasingly difficult to implement a causal therapy. But substantial therapeutic benefits may still be possible, notably if basic research can illuminate a "shortcut" between molecular intervention and systemic outcome. We think that in the present experiments with HD mice a rather robust motor response was induced by local (striatum), cell-selective (astrocytes) and artificial (EAAT2-S506X) transgene expression. Such result is to some extent surprising because most evidence-based models describe the initiation of voluntary movements as the result of a multi-level parallel and distributed information processing in a large number of brain structures (see for instance (Morita, 2014)). That a particular cell population can effectively control a set of motor acts has mostly been implicated in "lower" vertebrates or invertebrates.

However, reports on specific links between motor performance and specific transgene expression are already accumulating (see, for instance, (Nagai et al., 2019;Percie du et al., 2020)) and may help to identify new therapeutic targets. The present experiments will, hopefully, stimulate further investigation on the nature of signals involved in the regulation of EAAT2 sorting at synaptic sites. Notably, the dynamic balance between membrane insertion and protein degradation under the influence of second messengers will require further attention. Last, not least, the results have some promise with regard to small molecule therapy of neurologic conditions with hypokinesia, including Parkinson's disease, stroke and toxin-induced brain damage.

FIGURE CAPTIONS

Fig. 1. Identity and relative abundance of transduced cells. a Schematic illustration showing the type and sites of vector injection. **b-d** Specimens after triple labeling with representative astrocytic (b), neuronal **(c)** or microglial **(d)** markers, together with an antibody against mRuby3 and nuclear counterstaining with DAPI. **e** Transduced area visualized with mRuby3 on the background of DAPI (blue) and GFAP immunofluorescence (green). The putative margin of the striatum is marked with a dotted line. **f** The mRuby+ area at the indicated mediolatereral distance. **g** Incidence of transduced cells within the S100β-, NeuN- or Iba1-expressing cell populations. Numbers on columns: Evaluated sections and animals (in brackets). **h** Fraction of the astrocytic, neuronal or microglial phenotype among the mRuby3+ population in the dorsal striatum. Abbreviations: dSTR - dorsal striatum, M1-CTX - primary motor cortex (M1).

Fig. 2. Effects of bilateral EAAT2-S506X expression on the motor performance of Q175 mice. a Records of open field trajectories showing the mean running velocity between starts and stops (green or red circles, respectively). Gray coding of instantaneous running velocity. **b** Motor activity at rest. Color coding of movement velocity at rest. **c, d, f-k** Quantification of results from open field testing. **d, f** Step-over latency and its inverse relationship with the number of starts from rest. **l** matched age-, CAG- and body-weight composition of the test groups (only body weight illustrated).

Fig. 3. Rescue of glutamate uptake activity of striatal astrocytes after bilateral expression of EAAT2-S506X or EAAT2-4KR. a Measurement of glutamate uptake by sodium imaging with SBFI. Traces recorded in the absence and presence of TFB-TBOA (2 µM). The amplitude of this differential response was expressed as ΔF/F during the last 15 sec of L-Asp application. F is the mean fluorescence at rest, before drug application. **b** Averaged traces of SBFI fluorescence. Results from mRuby3-positive astrocytes only. **c** Quantification of the L-aspartate-induced sodium elevation. Two-level ("nested") statistics (animal level, cell level and posthoc comparison between groups). **d** The applied SBFI loading protocol was selective for astrocytes. Viewfield with 3 astrocytes, where one is transduced and two are not. **e** Traces from mRuby+ as opposed to mRuby- in three test groups. Averaged traces from one animal per group. **f** Comparison of results obtained in the different groups from mRuby3+ *vs.* mRuby3- astrocytes.

Fig. 4. Western blot analysis to examine HD-related changes in native murine EAAT2 and the effects elicited with EAAT2-S506X. a Basic scheme of mYFP-EAAT2 structure with the position of mYFP and the C-terminal truncation site. List of the injected vector constructs. **b** Region of vector injection and tissue collection. **c** Western blots for EAAT2 quantification in the striatal lysates from noninjected and EAAT2-injected WT. IR against EAAT2 (left panels) and mYFP (right panels). **d, e** Western blots for EAAT2 quantification in striatal lysates after immunostaining against EAAT2 and mYFP. Four animals per group (shown are two). Note the shifted position of the mYFP-EAAT2 band in EAAT2-S506X-injected mice and absence of corresponding band after staining of EAAT2 (boxed area). **f, g** Quantification of lysate stained with the EAAT2 or mYFP Abs. Note return of EAAT2 IR to

WT level although in this group the EAAT2 IR does not include the mYFP-EAAT2. mYFP expression levels were similar in the three animal groups. ANOVA and Tukey's multiple comparison test.

Fig. 5. Immunoprecipitation of mYFP and quantification of HD- and treatment-related changes in the abundance of mYFP-EAAT2 binders. a Scheme of experiment. **b** Results from 3 animal groups for comparison of full-length EAAT2 in WT *vs*. HET, and full-length EAAT2 *vs.* EAAT2-S506X (both in HET). Detection of mYFP in the immunoprecipitate. Note shift of the mYFP band in the mYFP-EAAT2-S505X group. **c** Quantification of results. The amount of mYFP is similar. **d** Quantification of HD- and treatment-related changes in the abundance of the mYFP-EAAT2 binders. Data from LFQ quantification. The same binders were found with iBAQ quantification. Only proteins with >3 peptides detection and abundance of log2 intensities >= 23 in all 4/5 animals of a group were included. The signal from each animal was normalized to the mYFP median intensity value in a histogram constructed from all samples. The inter-group intensities were compared by a two-tailed t-test. Empty bars: log2 difference (or FC ratio) of binder amounts in the HET-EAAT2 vs WT-EAAT2 groups. Bottom line: List of 20 interactors with significant HD-related difference (black asterisks on empty bars). An HD-related down-regulation is shown as downward bars, and an up-regulation - as upward bars. The same interactors were examined for changes between the HET-EAAT2-S506X *vs.* HET-EAAT2 groups (filled bars). In this case a significant change is denoted by green asterisks. The dashed bars denote the level required to reach WT levels. **e** Identification of 6 significant ($p<0.01$) EAAT2 interactors present both in WT and HET, but without effect of HD or C-terminal truncation. $p<0.05$ (*), $p<0.01$ (**) and $p<0.001$ (***).

Fig. 6. Rescue of single synapse glutamate clearance in the striatum after expression of EAAT2-S506X. a Specimens from single PT-type corticostriatal synaptic terminals in slices from WT, HET and treated HET. Bilateral intracranial injections of HET with EAAT2-S506X . The selected images were acquired at the response peak to illustrate the extension of $iGlu_u$ elevation (boxed area). Pink pixels within the black boundaries are pixels where stimulation of the bouton elicited a fluorescence increase (ΔF) to values larger than the resting level prior to stimulation (F). **b** Corresponding $iGlu_u$ values before and after electrical stimulation of the given bouton in the presence of TTX. The traces represent the mean value calculated from all suprathreshold pixels in the ROI. Red curves: Monoexponential functions fitted to the $iGlu_u$ traces. In black - respective time constants of decay (TauD). **c-e** Quantification of results. **f** Cumulative probability plot to illustrate the absence of TauD values >15 ms in WT and in EAAT2-S506X-treated HET. TauD values >15 ms identify pathological synapses in HET. **g** Only synapses in the immediate vicinity of transduced astrocytes were included, as confirmed by the location of the tested $iGlu_u$-expressing varicosity on the territory of mRuby3-positive astrocytes (arrowhead).

Fig. 7. Evaluation of synaptic EAAT2 immunofluorescence in fixed sections. a Confocal images from WT-CTRL and HET-CTRL to illustrate the HD-related decrease in the overall EAAT2 IF. In the illustrated samples the mean intensity values were 3078 ± 38.4 (WT-CTRL) and 2673 ± 31.7 (HET-CTRL). **b** Regions of interest (ROIs) comprising just one synapse. The ROIs correspond to the small boxed areas in **a**. The EAAT2-immunopositive area corresponds to an astrocyte PAP, as it is labeled with mRuby3. **c** Quantification of integral EAAT2 IF from ROIs comprising only one vGluT1-immunopositive terminal. Numbers in brackets: evaluated synapses per group. Each data point is the mean value from 30 synapses on 1 mRuby3-labeled astrocyte. 12 astrocytes per group from 2 mice/group.

METHODS

AAV plasmid design and vector production

Fig. 1 and Supplemental Tab. 2 present an overview of the used vectors, the sites of injections and the purpose of a chosen indicator. Plasmid pRcCMV-mYFP-EAAT2 and pRcCMV-mYFP-EAAT2-S506X were gifts from Christoph Fahlke and Arnd Baumann (Forschungszentrum Jülich). pRcCMV-mYFP-EAAT2 contains the expression cassette for the human *SLC1A2* fused to N-terminal mYFP. In pRcCMV-mYFP-EAAT2-S506X a serine at position 506 is point-mutated to generate a stop codon that causes the truncation of the last 68 amino acids of the C-terminus. This truncation does not interfere with the membrane insertion of the protein or glutamate transport (Leinenweber et al., 2011). In contrast, the mutation of four C-terminal lysine (Lys, K) residues to arginine (Arg, R) in the full-length EAAT2 has been shown to be critical for transporter internalization (Gonzalez-Gonzalez et al., 2008). Four consecutive cycles of site-directed mutagenesis were applied to generate EAAT2-4KR. In brief, pRcCMV-mYFP-EAAT2 was amplified by PCR using the mutagenesis primers listed in Supplemental Tab. 1, and the template was subsequently destroyed by DpnI digest. For high-effciency transformation, NEB C2987H® alpha-competent E. coli were incubated with the DpnI-digested PCR mix. Successful mutants were screened by Sanger sequencing (Eurofins Genomics, Köln). The expression cassettes for mYFP-EAAT2, mYFP-EAAT2-4KR and mYFP-EAAT2-S506X were subcloned by restriction digest with BamHI and EcoRI and ligation into a preexisting AAV backbone (pAAV-gfaABC1D-ChR2(LCTC)-p2a-FP635-WPRE) to produce pAAV-gfaABC1D-mYFP-EAAT2-WPRE, pAAV-gfaABC1D -mYFP-EAAT2-4KR-WPRE and pAAV-gfaABC1D -mYFP-EAAT2-S506X-WPRE. Monomeric mRuby3 was subcloned from pKanCMV-mRuby3-10aa-H2B into the three AAV vectors with AgeI and BsrGI to facilitate detection of the transduced astrocytes and the EGFP-based $iGlu_u$ in the corticostriatal terminals of the same preparation. Control vectors were constructed by amplifying mRuby3 or mYFP by PCR adding a 3' stop codon and a SalI restriction site and were then cloned into an AAV backbone to generate pAAV-gfaABC1D-mYFP-WPRE or pAAV-gfaABC1D-mRuby3-WPRE. The plasmids used or modified for further use are listed in Supplemental Tab. 1. The AAV vectors were produced at the Vector Core Facility of the Charité - University Medicine or at UPenn Vector Core. We acknowledge the contribution of Viviana Gradinaru and Benjamin Devermann for generating the PHP.eB adenoassociated virus (AAV) serotype (Chan et al., 2017).

Antibodies

The primary and secondary antibodies used for the quantification of Western blots or IR are also listed in Supplemental Tab. 2. For concentrations see the Methods section "Western blots and immunostaining". The EAAT2-Ab (Abcam, Cambridge, UK) was raised against a synthetic peptide within rat EAAT2 aa 550 to the C-terminus (C terminal) conjugated to keyhole limpet haemocyanin. The exact sequence is proprietary. Apart from several other C-terminus-directed Abs, we also tried Ab77039 and Ab203130 from Abcam were peptide fragments between aa143 and 239 were used as antigen but did not achieve the quality of immunostaing seen with Ab41621.

Animals

Z-Q175-KI mice were obtained from CHDI ("Cure Huntington's Disease Initiative", see stock # 027410 of the Jackson Laboratory, Bar Harbor, USA). All applicable international, national and institutional guidelines for the care and use of the animals were followed. The study design, performance of experiments and statistical evaluation has been approved by the Berlin Office of Health Protection and Technical Safety (G0218/17), with a yearly update of the experimental guidelines by the local authorities according to the 10 essential rules of ARRIVE (see latest update

from July 14, 2020 and (Percie du et al., 2020)). The experiments were performed in animals of either sex at an age of 51 to 76 weeks. The number of CAG repeats ranged from 182 to 201 and were determined by Laragen (Culver City, CA, USA). Care was taken that all experimental groups contained an equal number of males and females (±1). Apart from the body weight, no systematic differences could be detected in any of the evaluated indicators. Blinding was not applied, since the animals were used at a stage of HD when the experimenters could recognize the respective genotype and select the appropriate mice among a usually very small number of available animals. The necessary sample size was kept to a minimum and was calculated beforehand to achieve hypothesis testing at a significance level of 5%.

Stereotaxic and intravenous injections of viral expression vectors for treatment and diagnostic purposes

Q175 WT and HET were anaesthetized by intraperitoneal injection of a mixture containing 87.5 mg/kg ketamine and 12.5 mg/kg xylazine (both from Sigma-Aldrich, Taufkirchen) before receiving bilateral intrastriatal injections of PHP.eB-mRuby3-gfaABS1D-EAAT2 (or respective isoforms/controls) as part of the treatment. The therapeutic vectors or controls were given at a concentration of $1.0*10^{12}$ gc/ml and an amount of 1 µl per site ($1.0*10^{9}$gc/striatum) at the following coordinates with respect to bregma (mm): anterior 0.75, lateral 2.0, ventral 2.5. The intravenous injections (100 µl) were performed under slight isoflurane anaesthesia and adjusted to an injected amount of $2.0*10^{11}$ to $3.5*10^{11}$ gc/animal. The expression vector for the glutamate sensor AAV9-CamKII.iGlu$_u$.WPRE-hGH ($7.34*10^{13}$gc/ml - 0.3 µl) was applied at four sites at: anterior 1.5, lateral 1.56, 1.8, 2.04, 2.28 and ventral 1.7.

Behavioral tests in WT and Q175 HET

The animals were submitted to a classical open field test (53 cm x 33 cm), as described in a previous study with Q175 homozygotes (Rothe et al., 2015). The mice were individually tested between 9 a.m. and 2 p.m. using an open-field box made of gray plastic with 53 cm x 33 cm surface and 19 cm walls, illuminated by a spot of 25 W placed 1 m above the shadow-free box. Monitoring of 5-min sessions was done by a video camera (Logitech C525 Webcam, 15 frames/s). A customary software was designed to quantify not only running activity but also the motor activity at rest. This required the calculation of the centroid of all pixels derived from the black mouse body. To this end, the background frame without mouse was subtracted from frames with mouse using an intensity threshold of mean + 3SD. A virtual mouse radius (v.m.r.) was derived from the area of suprathreshold mouse pixels approximated as a circle. The identification of the resting state is based on the time needed to cross 2 v.m.r. For more details and definitions see Supplemental text.

For the "step-over test" the animal was placed into the center of a Petri dish (diameter 18.5 cm and wall height 2.8 cm). The movements were recorded with a video camera. Using offline analysis, a software routine determined the time between the take-off of the experimenter's hand (in a black glove) and the moment when the animal has reached the outside of the dish with all 4 feet. This parameter was called "step-over latency" and correlated with the open field total path in 5 min.

Extraction of GFP-tagged EAAT2 and interaction proteomics

The animals were anaesthetized with isoflurane, transcardially perfused with cooled aerated saline containing (in mM): N-methyl-D-glucamine chloride (NMDG) - 92, KCl - 2.5, NaH_2PO_4 - 1.25, $NaHCO_3$ - 25, glucose - 20, $CaCl_2$ - 0.5, $MgCl_2$ - 10, Na pyruvate - 3, and Na ascorbate - 5 (pH 7.35, 303 mosmol/l). If not mentioned otherwise, all chemicals and drugs mentioned here and in the following were obtained from Sigma-Aldrich (Taufkirchen). Brains were quickly removed, placed into a custom-made slicing mould and immersed into ice-cold oxygenated NMDG preparation solution. 2

mm thick sagittal slices where cut at a distance of 1-3 mm from midline. The striata were dissected and snap-frozen in liquid nitrogen. The tissue was pulverized under cryogenic conditions using a cryo-grinder set (CG 08-02, OPS Diagnostics, Lebanon, NJ, USA). The samples were solubilized in 200 µl lysis buffer containing (in mM) NaCl 150, Tris pH 7.5 50, n-ethylmaleimide 20, dithiothreitol (DTT) 1 supplemented with glycerol 5%, igepal ca-630 1% and Roche cOmplete protease inhibitor cocktail - 1x (all from Sigma-Aldrich). The samples were kept on ice for 30 min and homogenized at 5000 rpm for 10 sec every 10 min using a Polytron PT1300D homogenizer. Cell debris was removed by centrifugation at 14.000 x g for 10 min at 4 °C. The cleared lysate was diluted with 300 µl wash buffer (in mM) NaCl 150, Tris pH 7.5 50, DTT 1, glycerol 5% and incubated for 2 h with 30 µl of pre-washed GFP-Trap magnetic agarose beads (gtma-20, ChromoTek, Planegg-Martinsried) using gentle rotation at 4 °C. Protein complexes were isolated using a DynaMag-2 magnet (ThermoFisher Scientific), washed once in wash buffer containing igepal ca-630 0.05% and two more times in normal wash buffer before short-term storage of the samples at -18 °C.

The protein complex-containing beads were processed for analyses with liquid chromatography tandem mass spectrometry (LC-MS) as follows: digestion buffer (sodium deoxycholate - 1%, dithiothreitol - 10 mM, ammonium bicarbonate - 50 mM) was added to the beads for 45 min at room temperature. Proteins were submitted to alkylation with 55 mM chloroacetamide for 30 min in the dark at room temperature. 500 ng Endopeptidase LysC (Wako, Neuss) and 500 ng sequence grade trypsin (Promega, Mannheim, GER) was added and samples were digested over night at 37°C. Samples were acidified with formic acid (final concentration 1%) and peptides were extracted and desalted using the StageTips protocol. Peptides were separated by reversed phase chromatography on an in-house manufactured 20 cm fritless silica microcolumns with an inner diameter of 75 µm, packed with ReproSil-Pur C18-AQ 1.9 µm resin (Dr. Maisch GmbH, Ammerbuch), using a 98 min gradient with a 250 nl/min flow rate of increasing Buffer B concentration (from 2% to 60%, Buffer B: 90% acetonitrile) on an High Performance Liquid Chromatography (HPLC) system (ThermoFischer Scientific). Eluting peptides were directly ionized by electrospray ionization and transferred into a Thermo Orbitrap Fusion mass spectrometer. The instrument was operated in the data-dependent mode with performing full scans in Orbitrap (60K resolution; 4 x 10^5 ion count target; maximum injection time 50 ms), followed by top 20 MS2 scans using higher-energy collision dissociation (NCE of 32; 15K resolution, 5 x 10^4 ion count target; 0.7 m/z isolation window; maximum injection time: 250 ms). Only precursor with charge states between 2-7 were fragmented. Dynamic exclusion was set to 30 sec. Raw data were analyzed using the MaxQuant software (v1.6.0.1). The internal Andromeda search engine was used to search MS2 spectra against a decoy UniProt database for mouse (MOUSE.2018-05), as well as the sequences of the mYFP fusion constructs, containing forward and reverse sequences. The search included variable modifications of oxidation (M) and N-terminal acetylation, deamidation (N and Q) and fixed modification of carbamidomethyl cysteine. Minimal peptide length was set to 7 amino acids and a maximum of two missed cleavages was allowed. The false discovery rate (FDR) was set to 0.01 for peptide and protein identifications. The integrated label-free quantification and IBAQ calculation algorithm were activated. Unique and razor peptides were considered for quantification. Retention times were recalibrated based on the built-in nonlinear time-rescaling algorithm and MS/MS identifications were transferred between LC-MS/MS runs with the “Match between runs” option, in which the maximal retention time window was set to 0.7 min. The resulting text files were used for further analyses using the Perseus software package (omicX, v. 1.6.2.1). LFQ intensity values were used for quantification. Reverse hits, contaminants and proteins only identified by site were filtered out. Technical and biological replicates for each condition were defined as groups and intensity values were filtered for “minimum value of 3” per group. After log2 transformation missing values were imputed with random noise simulating the detection limit of the mass spectrometer. Imputed values are taken from a log normal distribution with 0.25× the standard

deviation of the measured, logarithmized values, down-shifted by 1.8 standard deviations. The data was obtained from 4 test groups, each comprising at least 4 animals per group. The signals obtained from any given animal (pooling the tissue from both striata) were normalized to the mYFP signal median intensity calculated from all samples. Only proteins with >3 peptide detection and abundance of log2 intensities >= 23 in all 4 samples were included. Differential protein abundance was calculated using two-sample Student´s t test, applying a permutation-based FDR cut-off at 1%. Abundance differences between the samples with a p-value of <=0.05 in a two-tailed t-test were considered significant.

Western blots

Samples were prepared according to the NuPAGE Technical Guide of Invitrogen. Briefly, samples were denatured in NuPAGE LDS sample buffer with DTT 50 mM for 10 min at 70 °C. The samples and markers were then run on a Novex bis-tris gradient gel (4-12%, ThermoFischer Scientific) using NuPAGE MOPS SDS running buffer and subsequently blotted on a Novex 0.45 µm nitrocellulose membrane (LC2001, ThermoFischer Scientific). The membranes were washed and blocked in ReadyTector solution A (CANDOR Bioscience GmbH, Wangen), and the primary antibodies rabbit anti-EAAT2 1:2000 (Abcam, Cambridge, UK) and mouse anti-GAPDH 1:1000 (Sigma-Aldrich) were directly applied for 1 h at room temperature in solution B that also contained horseradish peroxidase (HRP) coupled to the secondary antibodies against rabbit or mouse, respectively. To detect mYFP, membranes were blocked for 30 min in 1x Roti-block solution (Carl Roth GmbH, Karlsruhe) before applying rabbit anti-GFP 1:1000 (ChromoTek GmbH, Martinsried) over night at 4 °C in the same solution. Then the HRP-coupled secondary antibodies (Dianova GmbH, Hamburg) were applied at 1:2500 for 3 h at 4 °C. Proteins were detected using respective kits from Biozym Scientific GmbH (Hessisch Oldendorf).

Quantitative immunofluorescence (IF)

Using deep isoflurane anaesthesia, mice were transcardially perfused with 60 ml ice-cold phosphate-buffered saline (PBS) containing 4% (w/v) paraformaldehyde in PBS. Sagittal sections (30 µm) were prepared as previously described (Rothe et al., 2015). For the quantification of the transduction rate and transduction specificity freely floating sections were triple-stained with goat anti-tdTomato (also detects RFP variants like mRuby3) 1:6000 (Sicgen-Acris, Carcavelos), mouse anti S100□ 1:2000 (Novus, Abingdon) and rabbit anti-Iba1 1:1000 (Wako Chemicals GmbH, Neuss) or double-stained with goat anti-tdTomato and mouse anti-NeuN 1:500 (Merck Millipore, Darmstadt). Counter-staining for nuclei with 4′,6-diamidin-2-phenylindol (DAPI) 1:10000 was performed in both experiments. For the quantification of synaptic EAAT2 fluorescence, the sections were triple-stained with goat anti-tdTomato 1:6000 (Sicgen-Acris), guinea pig anti-vGluT1 1:1600 (Synaptic Systems, Göttingen) and rabbit anti-EAAT2 1:2000 (Abcam), followed by respective secondary antibodies, as listed in Supplemental Tab. 1. All sections from the different test groups were stained together for reliable comparison of EAAT2 IF levels.

RGB 24 bit images (1024 x 1024 pixels, pixel size 0.08 µm, 3x zoom, no binning) were acquired from the dorsal striatum using an inverted Leica DMI 6000 confocal microscope with an HCX PL Apo 63x oil objective (NA1.4) and stored in the tiff file format. Areas of interest (AOIs, 400 x 400 pixels) were cropped from the larger viewfields, selecting neuropil areas with a minimum of cell somatas or vessels. Quantification of EAAT2 IF was performed using ImagePro Plus (MediaCybernetics, Roper, Sarasota). For comparison purposes, the same staining conditions and acquisition settings were applied to achieve reliable EAAT2 quantification in 4-5 groups with at least 4 animals per group. Within the selected AOIs, smaller rectangular ROIs (25 x 25 pixels) were centred to individual vGluT1+ spots to determine the level of synaptic EAAT2 IF. A threshold algorithm was used to define the boundaries of

the EAAT2+ area excluding pixels with F< ROI mean + 0.5 SD. The data is expressed as integral intensity of suprathreshold pixels. The term “Synaptic integral EAAT2 IF” refers to the mean value from 30 individually assessed ROIs within the boundaries of one transduced (i.e. mRuby3+) astrocyte.

Preparation of acute brain slices

The animals were anaesthetized with isoflurane, transcardially perfused with cooled aerated saline containing (in mM): NMDG - 92, KCl - 2.5, NaH_2PO_4 - 1.25, $NaHCO_3$ - 25, glucose - 20, $CaCl_2$ - 0.5, $MgCl_2$ - 10, sodium pyruvate - 3, and sodium ascorbate - 5 (pH 7.35, 303 mosmol/l). After decapitation and removal of the brains, parasagittal (10 deg off) sections (300 µm) containing the striatum were prepared as previously described (Dvorzhak et al., 2016). The slices were kept in artificial cerebrospinal fluid (ACSF) containing (in mM): NaCl - 125, KCl - 3, NaH_2PO_4 - 1.25, $NaHCO_3$ - 25, $CaCl_2$ - 2, $MgCl_2$ - 1, glucose - 10 (pH 7.3, 303 mosmol/l), supplemented with (in mM) sodium pyruvate - 0.5, sodium ascorbate - 2.8 and glutathione - 0.005. These perfusion and recovery solutions preserved the astrocytes better than physiological ACSF, sucrose- or choline-containing solutions, the criterion being the astrocyte resting membrane potential at break-in WT (<= -75 mV).

***Ex vivo* sodium imaging in striatal astrocytes**

Our methods for sodium imaging in striatal astrocytes largely followed the techniques already described (Dvorzhak et al., 2016). Briefly, the slices were incubated for 20 - 30 min in oxygenated ACSF containing 222 µM of the membrane-permeable form of SBFI (#S-1264, ThermoFisherScientific), and 2.5% dimethyl sulfoxide (DMSO) and 0.5% Pluronic F-127 at 36°C. For recording of the L-aspartate-induced sodium transients, the gap junction blocker CBX (100 µM, Abcam) was added to the superfusion solution, along with blockers of ionotropic glutamate receptor blockers (DNQX 10 µM and MK801 1 µM, Tocris, Bristol, UK). Wide-field fluorescence imaging of SBFI-AM-stained slices was performed using a digital live acquisition imaging system (Andor Solis version 4.30.30034.0, Acal GmbH, Gröbenzell) and a sCMOS camera (Andor Zyla 4.2 plus) attached to an upright Zeiss microscope (Axio Examiner A1, Göttingen). Images were collected with a Zeiss 63x NA 1.0 water immersion plan apochromat objective. Cells were selected based on the resting levels of SBFI and mRuby3 fluorescence excited by a UVICO ultraviolet or visible light source (Rapp OptoElectronic, Hamburg), combined with suitable filter sets from Omega Optical (Brattleboro, VT, USA) attached to a FW 1000 filter wheel (Applied Scientific Instrumentation, Eugene, OR, USA). Single wavelength sodium imaging was performed by excitation of SBFI at 380 nm (sodium-sensitive wavelength). SBFI emission was collected at >510 nm (dichroic mirror XF2002, emission filter XF3086, Omega Optical). Regions of interest (ROIs) with a size of 3.2 µm x 3.2 µm were defined on the cell body. Binning was 8 x 8. The spatial resolution was then 0.8 µm/pixel. The exposure times was set to 150 msec in all experiments. Images were acquired every 3 sec. Custom-written software was used to control image acquisition and the valves operating the superfusion system. After 1 min of baseline recordings (20 images), L-aspartate (1 mM) was applied for 1 min followed by a 3 min washout period. Subsequently, the same routine was repeated in the presence of the glutamate transport blocker TFB-TBOA 2 µM (Tocris). For both traces the fluorescence change was calculated from the average of the baseline fluorescence intensities for each ROI as □F/F = (F_{SBFI} - $F_{SBFI(baseline)}$/$F_{SBFI(baseline)}$. The difference between the two traces represents the L-aspartate-induced sodium transient that is mediated by all available glutamate transporters. The response to L-aspartate was verified by student's t-test comparison between response peak and baseline.

***Ex vivo* glutamate imaging of corticostriatal synapses**

The methods established to image glutamate release from single corticostriatal presynaptic terminals and to identify synapses exhibiting an HD phenotype have already been described in some detail (Dvorzhak et al., 2019). Briefly, acute slices were submerged into a perfusion chamber with a constant

flow of oxygenated ACSF at a rate of 1-2 ml/min. The temperature during the recordings was maintained at 26 - 27 °C. Single varicosities expressing the ultrafast glutamate sensor $iGlu_u$ (Helassa et al., 2018) were visualized using a Zeiss wide field microscope (Axioscope 2, FS Plus) with a 63x /NA 1.0 water immersion objective and brief (180 ms) discontinuous exposure to a 473 nm laser beam focused to a circular area of ~4.5 µm in diameter. For evaluation of evoked responses, the $iGlu_u$ fluorescence was acquired at a frequency of 2.5 kHz from a rectangular ROI of 4 µm x 4 µm (20 x 20 pixels, binning 2) using a sCMOS camera (Andor Zyla4.2 plus). Laser, camera and electrical stimulation of the axon/bouton were controlled by in-house written software routines. Each pixel of the ROI was evaluated separately. The $iGlu_u$ pixel signal was expressed as change of fluorescence intensity □F in % of baseline fluorescence of the given pixel. The baseline is the mean of the intensity values obtained during the 50 ms period prior to stimulation. For the construction of time- and space-dependent [Glu] profiles after evoked release, suprathreshold pixels were determined, the threshold being defined as 3 SD of the ΔF/F baseline. The stimulus-induced changes of suprathreshold ΔF/F in time or space will be referred to as "$iGlu_u$ transients" or simply "transients". The term "Peak amplitude" refers to the peak ΔF/F value of an averaged intensity transient derived from all suprathreshold pixels. "Tau decay" or "TauD" is the time constant of decay derived by fitting a monoexponential function to the decay from the peak of the averaged transients. The spatial extension of the $iGlu_u$ signal is described on the basis of a virtual diameter derived from the area of all suprathreshold pixels combined to form a virtual circle. The area of suprathreshold pixels and the resulting virtual diameter were used as indicators of "Bouton size" (at rest, before stimulation) or "Spread" (after stimulation and glutamate release). The term "Peak spread" refers to the peak value of the averaged spread transient. Dysfunctional synapses could best be detected by analysis of single-pixel $iGlu_u$, using the pixel with the highest $iGlu_u$ elevation at any given terminal. The highest $iGlu_u$ elevations were always found within or next to the bouton at rest. The peak amplitude of the single pixel transient with the highest $iGlu_u$ elevation are referred to as "Maximal amplitude". The respective TauD values are referred to as "TauDmax".

Identification of dysfunctional synapses

To induce the glutamate release from individual synaptic boutons under physiological conditions, a depolarizing current pulse was applied through an ACSF-filled glass pipette (tip diameter <1 µM, resistance 10 MOhm) placed next to an axon in close proximity with a fluorescent varicosity. Responses were elicited at minimal intensity at a repetition frequency of 0.1 Hz. To challenge the glutamate uptake mechanisms at the site of release, individual synapses were stimulated under condition of blocked action potential generation (in the presence of tetrodotoxin, TTX, 1 µM and in elevated (5 mM) $[Ca^{2+}]_{ec}$. This standardized activation mode bypassed eventually existing disease-related differences in the myelination and excitability of corticostriatal axons. The identification of an HD phenotype in corticostriatal synapses is based on the TauD value of the glutamate transient (Dvorzhak et al., 2019).

Data evaluation and statistical analysis

The comparison of the means could be influenced by inter-animal variance. We therefore performed multi-level ("nested data") analysis using Prism 8 (GraphPad, San Diego, USA). P values of <0.05 were considered statistically significant. Significance levels were marked by asterisks, where * corresponds to P<0.05, ** - P<0.01 and *** - P<0.001. The numbers indicate animals, cells or presynaptic terminals, as mentioned in the figure legends or tables. Genotype-related effects are described in % of WT levels (Supplemental Tab. 1) or as effect strength according to Cohen's D or Hedges' G. D or G values larger 0.8 suggest that the respective effect was strong.

REFERENCE LIST

Al Awabdh S, Gupta-Agarwal S, Sheehan DF, Muir J, Norkett R, Twelvetrees AE, Griffin LD, Kittler JT (2016) Neuronal activity mediated regulation of glutamate transporter GLT-1 surface diffusion in rat astrocytes in dissociated and slice cultures. Glia 64: 1252-1264.

Beart PM, O'Shea RD (2007) Transporters for L-glutamate: an update on their molecular pharmacology and pathological involvement. Br J Pharmacol 150: 5-17.

Behrens PF, Franz P, Woodman B, Lindenberg KS, Landwehrmeyer GB (2002) Impaired glutamate transport and glutamate-glutamine cycling: downstream effects of the Huntington mutation. Brain 125: 1908-1922.

Berardelli A, Noth J, Thompson PD, Bollen EL, Curra A, Deuschl G, van Dijk JG, Topper R, Schwarz M, Roos RA (1999) Pathophysiology of chorea and bradykinesia in Huntington's disease. Mov Disord 14: 398-403.

Bergles DE, Jahr CE (1998) Glial contribution to glutamate uptake at Schaffer collateral- commissural synapses in the hippocampus. J Neurosci 18: 7709-7716.

Bradford J, Shin JY, Roberts M, Wang CE, Li XJ, Li S (2009) Expression of mutant huntingtin in mouse brain astrocytes causes age-dependent neurological symptoms. Proc Natl Acad Sci U S A 106: 22480-22485.

Burgold J, Schulz-Trieglaff EK, Voelkl K, Gutierrez-Angel S, Bader JM, Hosp F, Mann M, Arzberger T, Klein R, Liebscher S, Dudanova I (2019) Cortical circuit alterations precede motor impairments in Huntington's disease mice. Sci Rep 9: 6634-43024.

Carrillo-Reid L, Day M, Xie Z, Melendez AE, Kondapalli J, Plotkin JL, Wokosin DL, Chen Y, Kress GJ, Kaplitt M, Ilijic E, Guzman JN, Chan CS, Surmeier DJ (2019) Mutant huntingtin enhances activation of dendritic Kv4 K(+) channels in striatal spiny projection neurons. Elife 8. pii: 40818.

Chai H, Diaz-Castro B, Shigetomi E, Monte E, Octeau JC, Yu X, Cohn W, Rajendran PS, Vondriska TM, Whitelegge JP, Coppola G, Khakh BS (2017) Neural circuit-specialized astrocytes: Transcriptomic, proteomic, morphological, and functional evidence. Neuron 95: 531-549.

Chan KY, Jang MJ, Yoo BB, Greenbaum A, Ravi N, Wu WL, SÃ¡nchez-Guardado L, Lois C, Mazmanian SK, Deverman BE, Gradinaru V (2017) Engineered AAVs for efficient noninvasive gene delivery to the central and peripheral nervous systems. Nat Neurosci 20: 1172-1179.

Danbolt NC (2001) Glutamate uptake. Prog Neurobiol 65: 1-105.

Deng YP, Wong T, Bricker-Anthony C, Deng B, Reiner A (2013) Loss of corticostriatal and thalamostriatal synaptic terminals precedes striatal projection neuron pathology in heterozygous Q140 Huntington's disease mice. Neurobiol Dis 60: 89-107.

Dvorzhak A, Helassa N, Torok K, Schmitz D, Grantyn R (2019) Single synapse indicators of impaired glutamate clearance derived from fast iGlu*u* imaging of cortical afferents in the striatum of normal and Huntington (Q175) mice. J Neurosci 39: 3970-3982.

Dvorzhak A, Vagner T, Grantyn R (2016) Functional indicators of glutamate transport in single striatal astrocytes and the influence of Kir4.1 in normal and Huntington mice. J Neurosci 16: 4959-4975.

Enger R, Gundersen GA, Haj-Yasein NN, Eilert-Olsen M, Thoren AE, Vindedal GF, Petersen PH, Skare O, Nedergaard M, Ottersen OP, Nagelhus EA (2012) Molecular scaffolds underpinning macroglial polarization: an analysis of retinal Muller cells and brain astrocytes in mouse. Glia 60: 2018-2026.

Faideau M, Kim J, Cormier K, Gilmore R, Welch M, Auregan G, Dufour N, Guillermier M, Brouillet E, Hantraye P, Deglon N, Ferrante RJ, Bonvento G (2010) In vivo expression of polyglutamine-expanded huntingtin by mouse striatal astrocytes impairs glutamate transport: a correlation with Huntington's disease subjects. Hum Mol Genet 19: 3053-3067.

Foran E, Bogush A, Goffredo M, Roncaglia P, Gustincich S, Pasinelli P, Trotti D (2011) Motor neuron impairment mediated by a sumoylated fragment of the glial glutamate transporter EAAT2. Glia 59: 1719-1731.

Ghosh M, Lane M, Krizman E, Sattler R, Rothstein JD, Robinson MB (2016) The transcription factor Pax6 contributes to the induction of GLT-1 expression in astrocytes through an interaction with a distal enhancer element. J Neurochem 136: 262-275.

Gibb SL, Boston-Howes W, Lavina ZS, Gustincich S, Brown RH, Jr., Pasinelli P, Trotti D (2007) A caspase-3-cleaved fragment of the glial glutamate transporter EAAT2 is sumoylated and targeted to promyelocytic leukemia nuclear bodies in mutant SOD1-linked amyotrophic lateral sclerosis. J Biol Chem 282: 32480-32490.

Gonzalez-Gonzalez IM, Garcia-Tardon N, Gimenez C, Zafra F (2008) PKC-dependent endocytosis of the GLT1 glutamate transporter depends on ubiquitylation of lysines located in a C-terminal cluster. Glia 56: 963-974.

Hart EP, Marinus J, Burgunder JM, Bentivoglio AR, Craufurd D, Reilmann R, Saft C, Roos RA (2013) Better global and cognitive functioning in choreatic versus hypokinetic-rigid Huntington's disease. Mov Disord 28: 1142-1145.

Helassa N, Durst CD, Coates C, Kerruth S, Arif U, Schulze C, Wiegert JS, Geeves M, Oertner TG, Torok K (2018) Ultrafast glutamate sensors resolve high-frequency release at Schaffer collateral synapses. Proc Natl Acad Sci U S A 115: 5594-5599.

Horton MC, Nopoulos P, Nance M, Landwehrmyer GB, Barker RA, Squitieri F, Burgunder JM, Quarrell O (2019) Assessment of the performance of a modified motor scale as applied to juvenile onset Huntington's disease. J Huntingtons Dis 8: 181-193.

Huang K, Kang MH, Askew C, Kang R, Sanders SS, Wan J, Davis NG, Hayden MR (2010) Palmitoylation and function of glial glutamate transporter-1 is reduced in the YAC128 mouse model of Huntington disease. Neurobiol Dis 40: 207-215.

Ibanez I, Diez-Guerra FJ, Gimenez C, Zafra F (2016) Activity dependent internalization of the glutamate transporter GLT-1 mediated by beta-arrestin 1 and ubiquitination. Neuropharmacol 107: 376-386.

Kaemmerer WF, Grondin RC (2019) The effects of huntingtin-lowering: what do we know so far? Degener Neurol Neuromuscul Dis 9: 3-17.

Kalandadze A, Wu Y, Robinson MB (2002) Protein kinase C activation decreases cell surface expression of the GLT-1 subtype of glutamate transporter. Requirement of a carboxyl-terminal domain and partial dependence on serine 486. J Biol Chem 277: 45741-45750.

Kirschner MA, Copeland NG, Gilbert DJ, Jenkins NA, Amara SG (1994) Mouse excitatory amino acid transporter EAAT2: isolation, characterization, and proximity to neuroexcitability loci on mouse chromosome 2. Genomics 24: 218-224.

Lee SG, Su ZZ, Emdad L, Gupta P, Sarkar D, Borjabad A, Volsky DJ, Fisher PB (2008) Mechanism of ceftriaxone induction of excitatory amino acid transporter-2 expression and glutamate uptake in primary human astrocytes. J Biol Chem 283: 13116-13123.

Lehre KP, Danbolt NC (1998) The number of glutamate transporter subtype molecules at glutamatergic synapses: Chemical and stereological quantification in young adult rat brain. J Neurosci 18: 8751-8757.

Leinenweber A, Machtens JP, Begemann B, Fahlke C (2011) Regulation of glial glutamate transporters by C-terminal domains. J Biol Chem 286: 1927-1937.

Lievens JC, Woodman B, Mahal A, Spasic-Boscovic O, Samuel D, Kerkerian-Le Goff L, Bates GP (2001) Impaired glutamate uptake in the R6 Huntington's disease transgenic mice. Neurobiol Dis 8: 807-821.

Martinez-Villarreal J, Garcia TN, Ibanez I, Gimenez C, Zafra F (2012) Cell surface turnover of the glutamate transporter GLT-1 is mediated by ubiquitination/deubiquitination. Glia 60: 1356-1365.

Menalled LB, Kudwa AE, Miller S, Fitzpatrick J, Watson-Johnson J, Keating N, Ruiz M, Mushlin R, Alosio W, McConnell K, Connor D, Murphy C, Oakeshott S, Kwan M, Beltran J, Ghavami A, Brunner D, Park LC, Ramboz S, Howland D (2012) Comprehensive behavioral and molecular characterization of a new knock-in mouse model of Huntington's disease: zQ175. PLoS One 7: e49838.

Merienne N, Vachey G, de Longprez L, Meunier C, Zimmer V, Perriard G, Canales M, Mathias A, Herrgott L, Beltraminelli T, Maulet A, Dequesne T, Pythoud C, Rey M, Pellerin L, Brouillet E, Perrier AL, du PR, Deglon N (2017) The Self-Inactivating KamiCas9 System for the Editing of CNS Disease Genes. Cell Rep 20: 2980-2991.

Meunier C, Merienne N, Jolle C, Deglon N, Pellerin L (2016) Astrocytes are key but indirect contributors to the development of the symptomatology and pathophysiology of Huntington's disease. Glia 64: 1841-1856.

Miller BR, Dorner JL, Bunner KD, Gaither TW, Klein EL, Barton SJ, Rebec GV (2012) Up-regulation of GLT1 reverses the deficit in cortically evoked striatal ascorbate efflux in the R6/2 mouse model of Huntington's disease. J Neurochem 121: 629-638.

Miller BR, Dorner JL, Shou M, Sari Y, Barton SJ, Sengelaub DR, Kennedy RT, Rebec GV (2008) Up-regulation of GLT1 expression increases glutamate uptake and attenuates the Huntington's disease phenotype in the R6/2 mouse. Neurosci 153: 329-337.

Morita K (2014) Differential cortical activation of the striatal direct and indirect pathway cells: reconciling the anatomical and optogenetic results by using a computational method. J Neurophysiol 112: 120-146.

Mrzljak L, Munoz-Sanjuan I (2015) Therapeutic Strategies for Huntington's Disease. Curr Top Behav Neurosci 22: 161-201.

Mullard A (2019) Pioneering antisense drug heads into pivotal trials for Huntington disease. Nat Rev Drug Discov 18: 161-163.

Murphy-Royal C, Dupuis JP, Varela JA, Panatier A, Pinson B, Baufreton J, Groc L, Oliet SH (2015) Surface diffusion of astrocytic glutamate transporters shapes synaptic transmission. Nat Neurosci 18: 219-226.

Nagai J, Rajbhandari AK, Gangwani MR, Hachisuka A, Coppola G, Masmanidis SC, Fanselow MS, Khakh BS (2019) Hyperactivity with Disrupted Attention by Activation of an Astrocyte Synaptogenic Cue. Cell 177: 1280-1292.

Octeau JC, Chai H, Jiang R, Bonanno SL, Martin KC, Khakh BS (2018) An optical neuron-astrocyte proximity assay at synaptic distance scales. Neuron 98: 49-66.

Parsons MP, Vanni MP, Woodard CL, Kang R, Murphy TH, Raymond LA (2016) Real-time imaging of glutamate clearance reveals normal striatal uptake in Huntington disease mouse models. Nat Commun 7: 11251.

Percie du SN, Ahluwalia A, Alam S, Avey MT, Baker M, Browne WJ, Clark A, Cuthill IC, Dirnagl U, Emerson M, Garner P, Holgate ST, Howells DW, Hurst V, Karp NA, Lazic SE, Lidster K, MacCallum CJ, Macleod M, Pearl EJ, Petersen OH, Rawle F, Reynolds P, Rooney K, Sena ES, Silberberg SD, Steckler T, WÃ¼rbel H (2020) Reporting animal research: Explanation and elaboration for the ARRIVE guidelines 2.0. PLoS Biol 18: e3000411.

Plotkin JL, Day M, Peterson JD, Xie Z, Kress GJ, Rafalovich I, Kondapalli J, Gertler TS, Flajolet M, Greengard P, Stavarache M, Kaplitt MG, Rosinski J, Chan CS, Surmeier DJ (2014) Impaired TrkB receptor signaling underlies corticostriatal dysfunction in Huntington's disease. Neuron 83: 178-188.

Plotkin JL, Surmeier DJ (2015) Corticostriatal synaptic adaptations in Huntington's disease. Curr Opin Neurobiol 33C: 53-62.

Reiner A, Deng YP (2018) Disrupted striatal neuron inputs and outputs in Huntington's disease. CNS Neurosci Ther 24: 250-280.

Rosenblatt A, Abbott MH, Gourley LM, Troncoso JC, Margolis RL, Brandt J, Ross CA (2003) Predictors of neuropathological severity in 100 patients with Huntington's disease. Ann Neurol 54: 488-493.

Rosenblum LT, Shamamandri-Markandaiah S, Ghosh B, Foran E, Lepore AC, Pasinelli P, Trotti D (2017) Mutation of the caspase-3 cleavage site in the astroglial glutamate transporter EAAT2 delays disease progression and extends lifespan in the SOD1-G93A mouse model of ALS. Exp Neurol 292: 145-153.

Rothe T, Deliano M, Wojtowicz AM, Dvorzhak A, Harnack D, Paul S, Vagner T, Melnick I, Stark H, Grantyn R (2015) Pathological gamma oscillations, impaired dopamine release, synapse loss and reduced dynamic range of unitary glutamatergic synaptic transmission in the striatum of hypokinetic Q175 Huntington mice. Neurosci 311: 519-538.

Sato J, Horibe S, Kawauchi S, Sasaki N, Hirata KI, Rikitake Y (2018) Involvement of aquaporin-4 in laminin-enhanced process formation of mouse astrocytes in 2D culture: Roles of dystroglycan and alpha-syntrophin in aquaporin-4 expression. J Neurochem 147: 495-513.

Shin JY, Fang ZH, Yu ZX, Wang CE, Li SH, Li XJ (2005) Expression of mutant huntingtin in glial cells contributes to neuronal excitotoxicity. J Cell Biol 171: 1001-1012.

Spuler S, Krug H, Klein C, Medialdea IC, Jakob W, Ebersbach G, Gruber D, Hoffmann KT, Trottenberg T, Kupsch A (2010) Myopathy causing camptocormia in idiopathic Parkinson's disease: a multidisciplinary approach. Mov Disord 25: 552-559.

Steffan JS, Agrawal N, Pallos J, Rockabrand E, Trotman LC, Slepko N, Illes K, Lukacsovich T, Zhu YZ, Cattaneo E, Pandolfi PP, Thompson LM, Marsh JL (2004) SUMO modification of huntingtin and Huntington's disease pathology. Science 304: 100-104.

Sullivan R, Rauen T, Fischer F, Wiessner M, Grewer C, Bicho A, Pow DV (2004) Cloning, transport properties, and differential localization of two splice variants of GLT-1 in the rat CNS: implications for CNS glutamate homeostasis. Glia 45: 155-169.

Tabrizi SJ, Ghosh R, Leavitt BR (2019) Huntingtin lowering strategies for disease modification in Huntington's disease. Neuron 101: 801-819.

Tabrizi SJ, Scahill RI, Owen G, Durr A, Leavitt BR, Roos RA, Borowsky B, Landwehrmeyer B, Frost C, Johnson H, Craufurd D, Reilmann R, Stout JC, Langbehn DR (2013) Predictors of phenotypic progression and disease onset in premanifest and early-stage Huntington's disease in the TRACK-HD study: analysis of 36-month observational data. Lancet Neurol 12: 637-649.

Underhill SM, Wheeler DS, Amara SG (2015) Differential regulation of two isoforms of the glial glutamate transporter EAAT2 by DLG1 and CaMKII. J Neurosci 35: 5260-5270.

Vandenberg RJ, Ryan RM (2013) Mechanisms of glutamate transport. Physiol Rev 93: 1621-1657.

Veldman MB, Yang XW (2018) Molecular insights into corticostriatal miscommunications in Huntington's disease. Curr Opin Neurobiol 48: 79-89.

Zeitler B, Froelich S, Marlen K, Shivak DA, Yu Q, Li D, Pearl JR, Miller JC, Zhang L, Paschon DE, Hinkley SJ, Ankoudinova I, Lam S, Guschin D, Kopan L, Cherone JM, Nguyen HB, Qiao G, Ataei Y, Mendel MC, Amora R, Surosky R, Laganiere J, Vu BJ, Narayanan A, Sedaghat Y, Tillack K, Thiede C, Gartner A, Kwak S, Bard J, Mrzljak L, Park L, Heikkinen T, Lehtimaki KK, Svedberg MM, Haggkvist J, Tari L, Toth M, Varrone A, Halldin C, Kudwa AE, Ramboz S, Day M, Kondapalli J, Surmeier DJ, Urnov FD, Gregory PD, Rebar EJ, Munoz-Sanjuan I, Zhang HS (2019) Allele-selective transcriptional repression of mutant HTT for the treatment of Huntington's disease. Nat Med 25: 1131-1142.

Zhang Y, He X, Meng X, Wu X, Tong H, Zhang X, Qu S (2017) Regulation of glutamate transporter trafficking by Nedd4-2 in a Parkinson's disease model. Cell Death Dis 8: e2574.

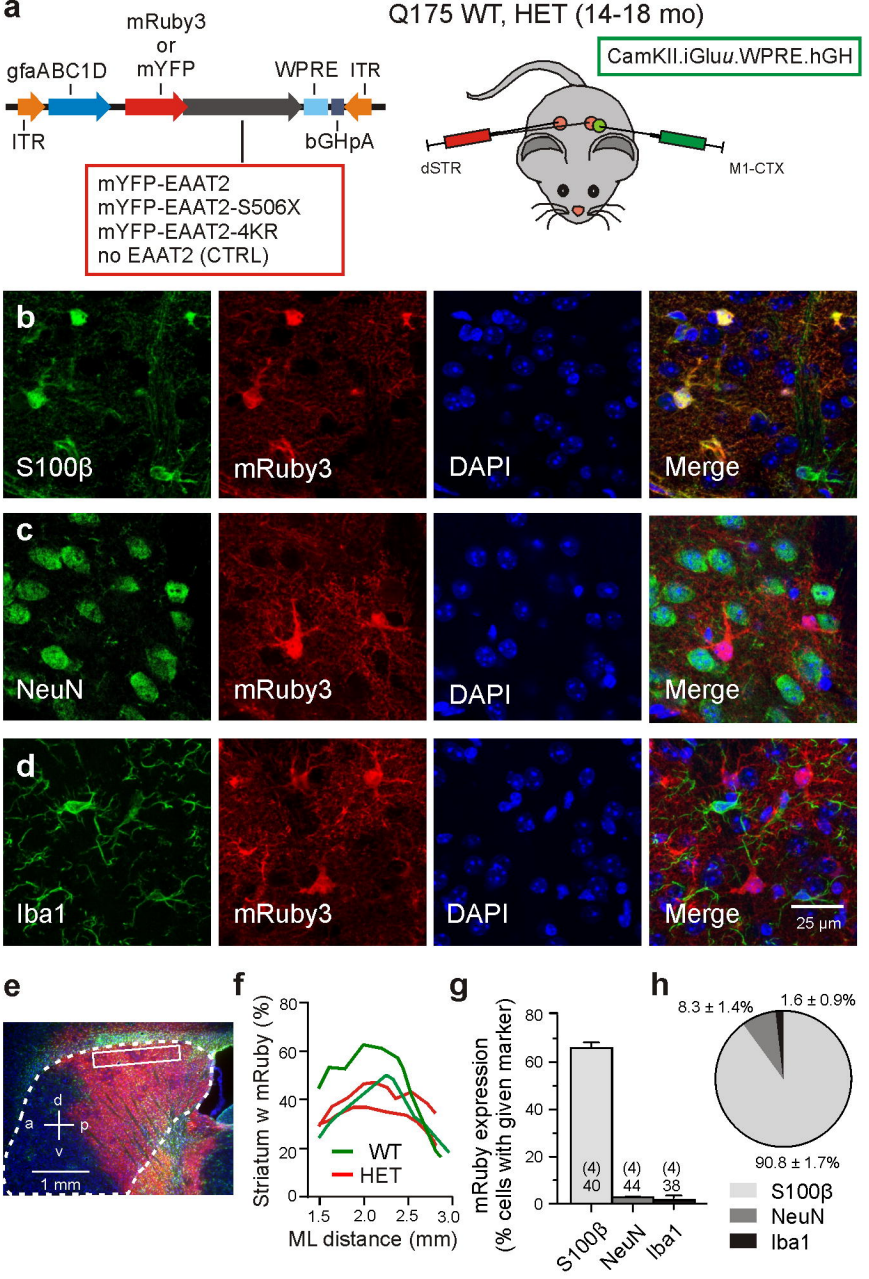

Fig. 1. Identity and relative abundance of transduced cells. a *Schematic illustration showing the type and sites of vector injection.* ***b-d*** *Specimens after triple labeling with representative astrocytic (b), neuronal* ***(c)*** *or microglial* ***(d)*** *markers, together with an antibody against mRuby3 and nuclear counterstaining with DAPI.* ***e*** *Transduced area visualized with mRuby3 on the background of DAPI (blue) and GFAP immunofluorescence (green). The putative margin of the striatum is marked with a dotted line.* ***f*** *The mRuby+ area at the indicated mediolatereral distance.* ***g*** *Incidence of transduced cells within the S100β-, NeuN- or Iba1-expressing cell populations. Numbers on columns: Evaluated sections and animals (in brackets).* ***h*** *Fraction of the astrocytic, neuronal or microglial phenotype among the mRuby3+ population in the dorsal striatum. Abbreviations: dSTR - dorsal striatum, M1-CTX - primary motor cortex (M1).*

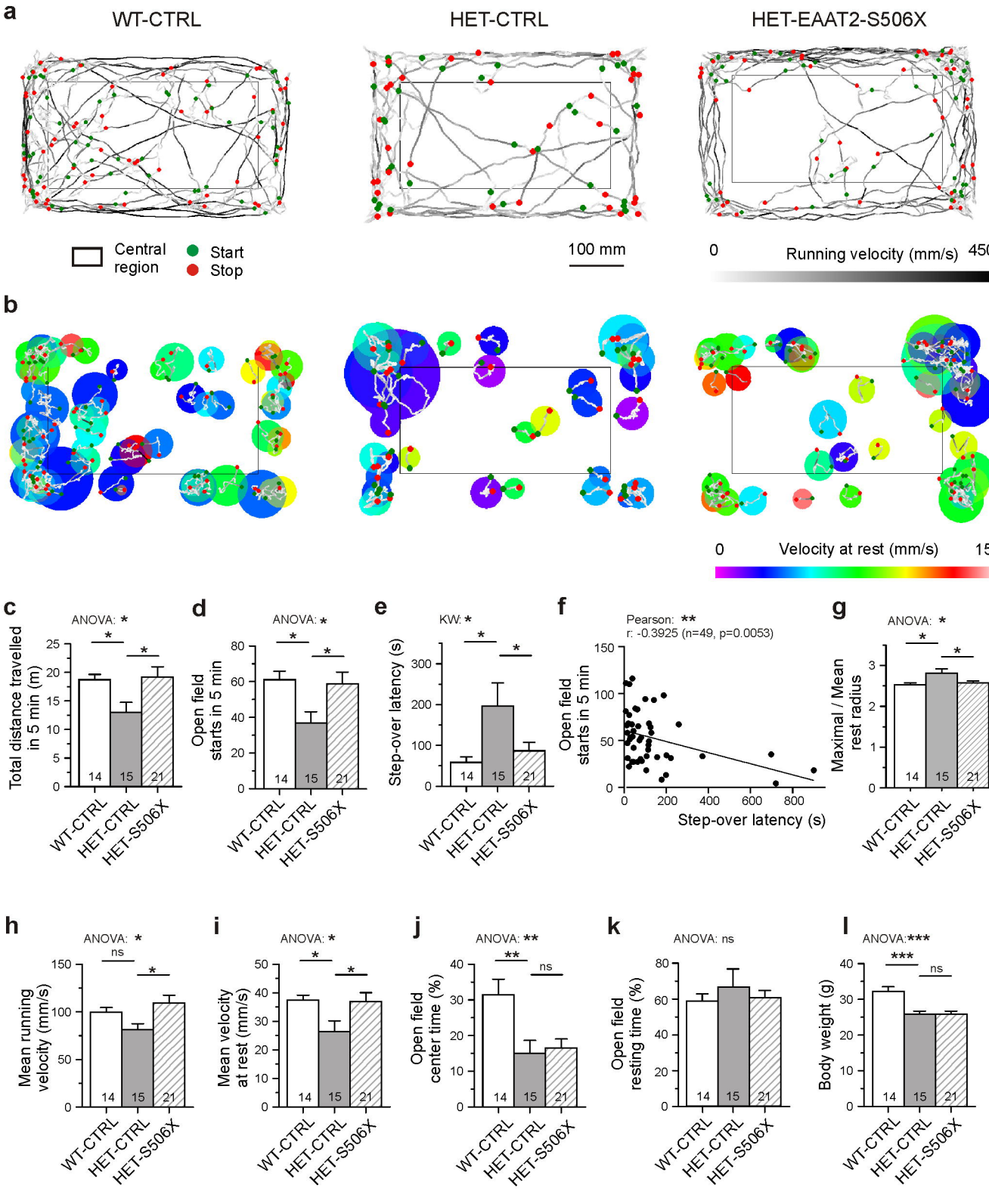

Fig. 2. Effects of bilateral EAAT2-S506X expression on the motor performance of Q175 mice. a *Records of open field trajectories showing the mean running velocity between starts and stops (green or red circles, respectively). Gray coding of instantaneous running velocity.* ***b*** *Motor activity at rest. Color coding of movement velocity at rest.* ***c, d, f-k*** *Quantification of results from open field testing.* ***d, f*** *Step-over latency and its inverse relationship with the number of starts from rest.* ***l*** *matched age-, CAG- and body-weight composition of the test groups (only body weight illustrated).*

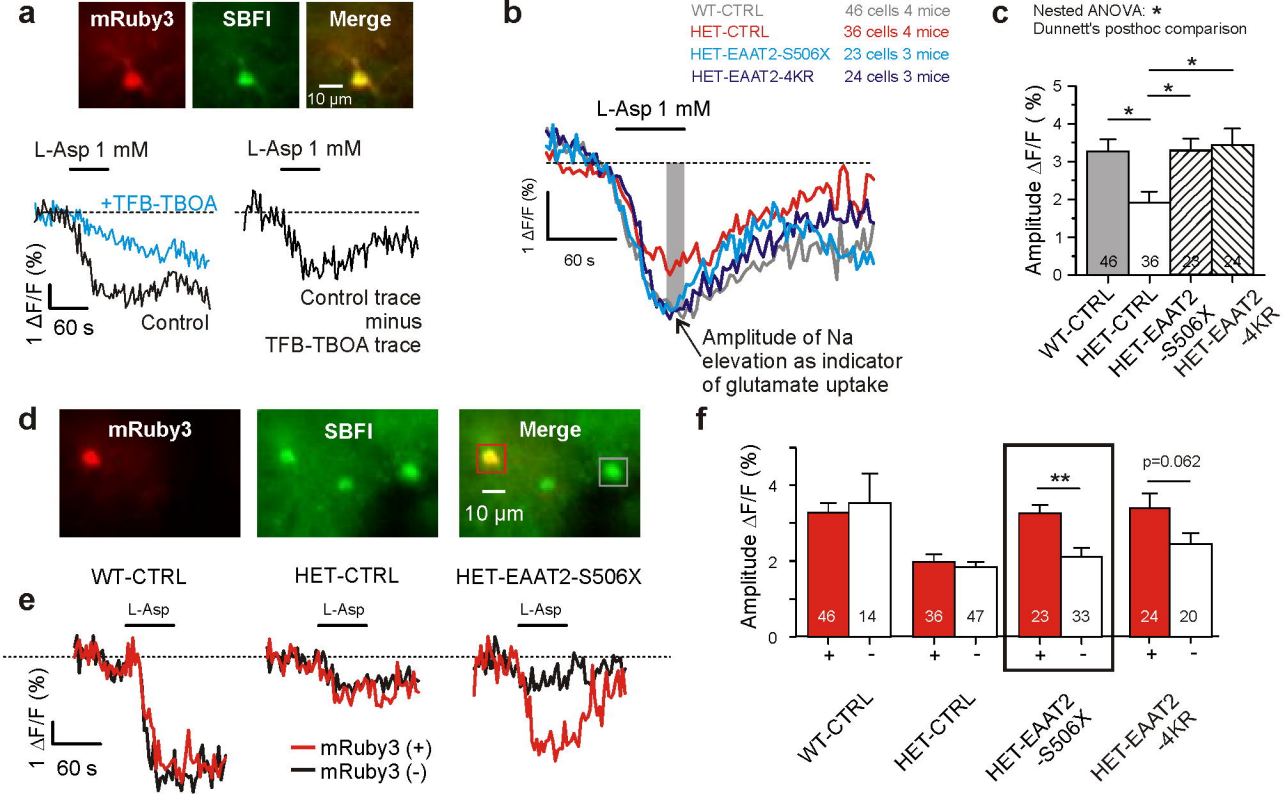

Fig. 3. Rescue of glutamate uptake activity of striatal astrocytes after bilateral expression of EAAT2-S506X or EAAT2-4KR. ***a*** *Measurement of glutamate uptake by sodium imaging with SBFI. Traces recorded in the absence and presence of TFB-TBOA (2 µM). The amplitude of this differential response was expressed as ΔF/F during the last 15 sec of L-Asp application. F is the mean fluorescence at rest, before drug application.* ***b*** *Averaged traces of SBFI fluorescence. Results from mRuby3-positive astrocytes only.* ***c*** *Quantification of the L-aspartate-induced sodium elevation. Two-level ("nested") statistics (animal level, cell level and posthoc comparison between groups).* ***d*** *The applied SBFI loading protocol was selective for astrocytes. Viewfield with 3 astrocytes, where one is transduced and two are not.* ***e*** *Traces from mRuby+ as opposed to mRuby- in three test groups. Averaged traces from one animal per group.* ***f*** *Comparison of results obtained in the different groups from mRuby3+ vs. mRuby3- astrocytes.*

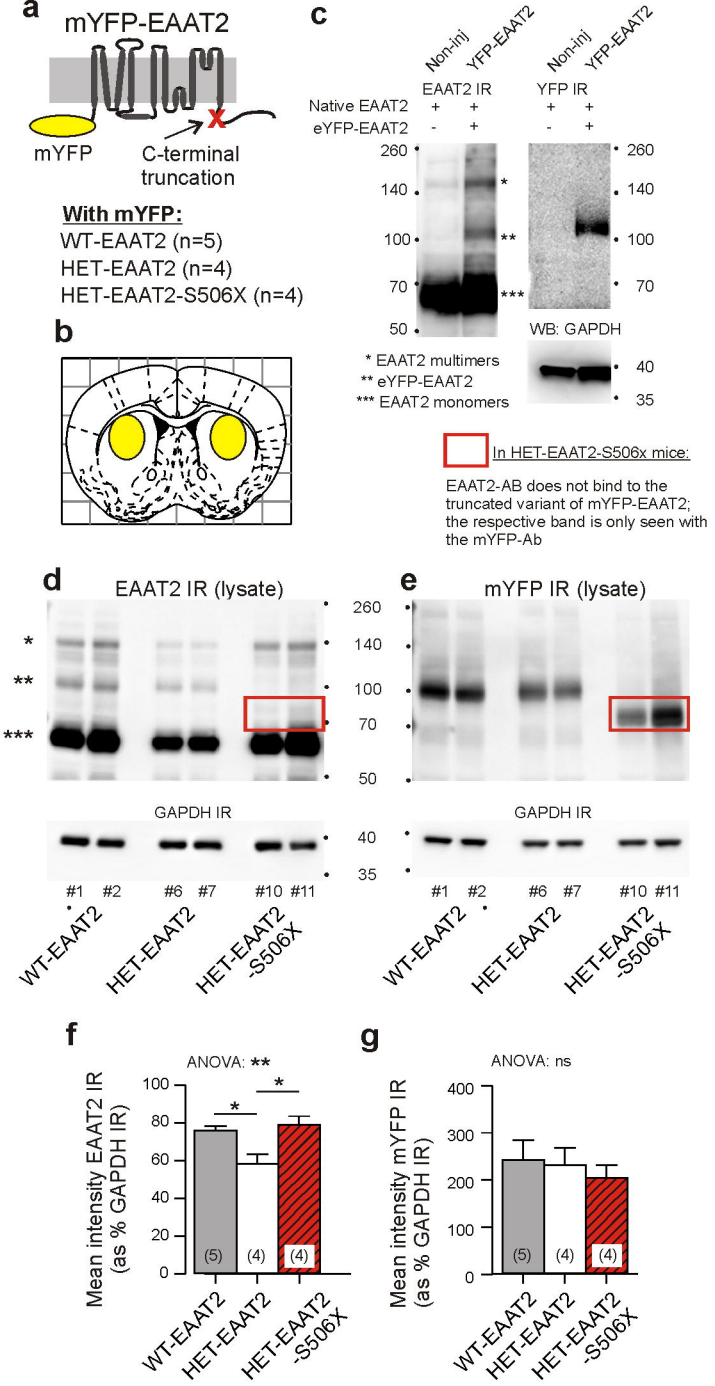

Fig. 4. Western blot analysis to examine HD-related changes in native murine EAAT2 and the effects elicited with EAAT2-S506X. ***a*** *Basic scheme of mYFP-EAAT2 structure with the position of mYFP and the C-terminal truncation site. List of the injected vector constructs.* ***b*** *Region of vector injection and tissue collection.* ***c*** *Western blots for EAAT2 quantification in the striatal lysates from noninjected and EAAT2-injected WT. IR against EAAT2 (left panels) and mYFP (right panels).* ***d, e*** *Western blots for EAAT2 quantification in striatal lysates after immunostaining against EAAT2 and mYFP. Two animals per group. Note the shifted position of the mYFP-EAAT2 band in EAAT2-S506X-injected mice and absence of corresponding band after staining of EAAT2 (boxed area).* ***f, g*** *Quantification of lysate staining with the EAAT2 or mYFP antibodies. Note recovery of EAAT2 IR to WT level although in this group the EAAT2 IR does not include the mYFP-EAAT2. mYFP expression levels were similar in the three animal groups. ANOVA and Tukey's multiple comparison test.*

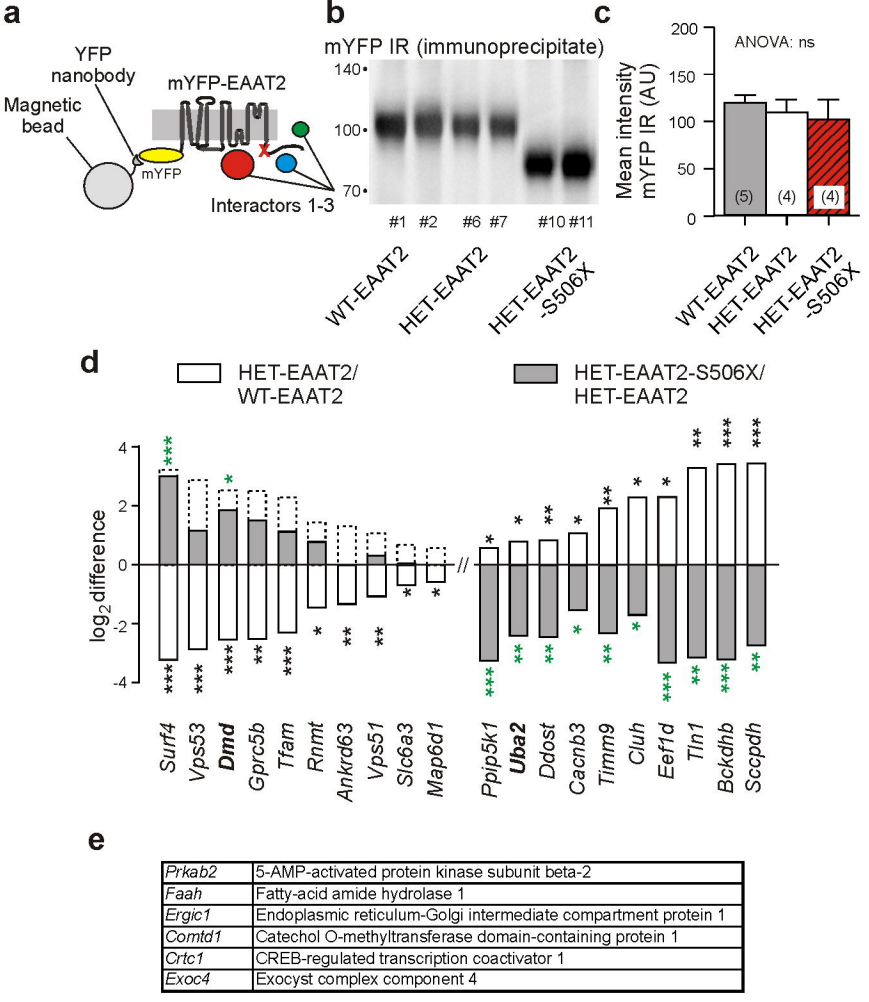

Prkab2	5-AMP-activated protein kinase subunit beta-2
Faah	Fatty-acid amide hydrolase 1
Ergic1	Endoplasmic reticulum-Golgi intermediate compartment protein 1
Comtd1	Catechol O-methyltransferase domain-containing protein 1
Crtc1	CREB-regulated transcription coactivator 1
Exoc4	Exocyst complex component 4

Fig. 5. Immunoprecipitation of mYFP and quantification of HD- and treatment-related changes in the abundance of mYFP-EAAT2 binders. a *Scheme of experiment.* ***b*** *Results from 3 animal groups for comparison of full-length EAAT2 in WT vs. HET, and full-length EAAT2 vs. EAAT2-S506X (both in HET). Detection of mYFP in the immunoprecipitate. Note shift of the mYFP band in the mYFP-EAAT2-S505X group.* ***c*** *Quantification of results. The amount of mYFP is similar.* ***d*** *Quantification of HD- and treatment-related changes in the abundance of the mYFP-EAAT2 binders. Data from LFQ quantification. The same binders were found with iBAQ quantification. Only proteins with >3 peptides detection and abundance of log2 intensities >= 23 in all 4/5 animals of a group were included. The signal from each animal was normalized to the mYFP median intensity value in a histogram constructed from all samples. The inter-group intensities were compared by a two-tailed t-test. Empty bars: log2 difference (or FC ratio) of binder amounts in the HET-EAAT2 vs WT-EAAT2 groups. Bottom line: List of 20 interactors with significant HD-related difference (black asterisks on empty bars). An HD-related down-regulation is shown as downward bars, and an up-regulation - as upward bars. The same interactors were examined for changes between the HET-EAAT2-S506X vs. HET-EAAT2 groups (filled bars). In this case a significant change is denoted by green asterisks. The dashed bars denote the level required to reach WT levels.* ***e*** *Identification of 6 significant (p<0.01) EAAT2 interactors present both in WT and HET, but without effect of HD or C-terminal truncation. p<0.05 (*), p<0.01 (**) and p<0.001 (***).*

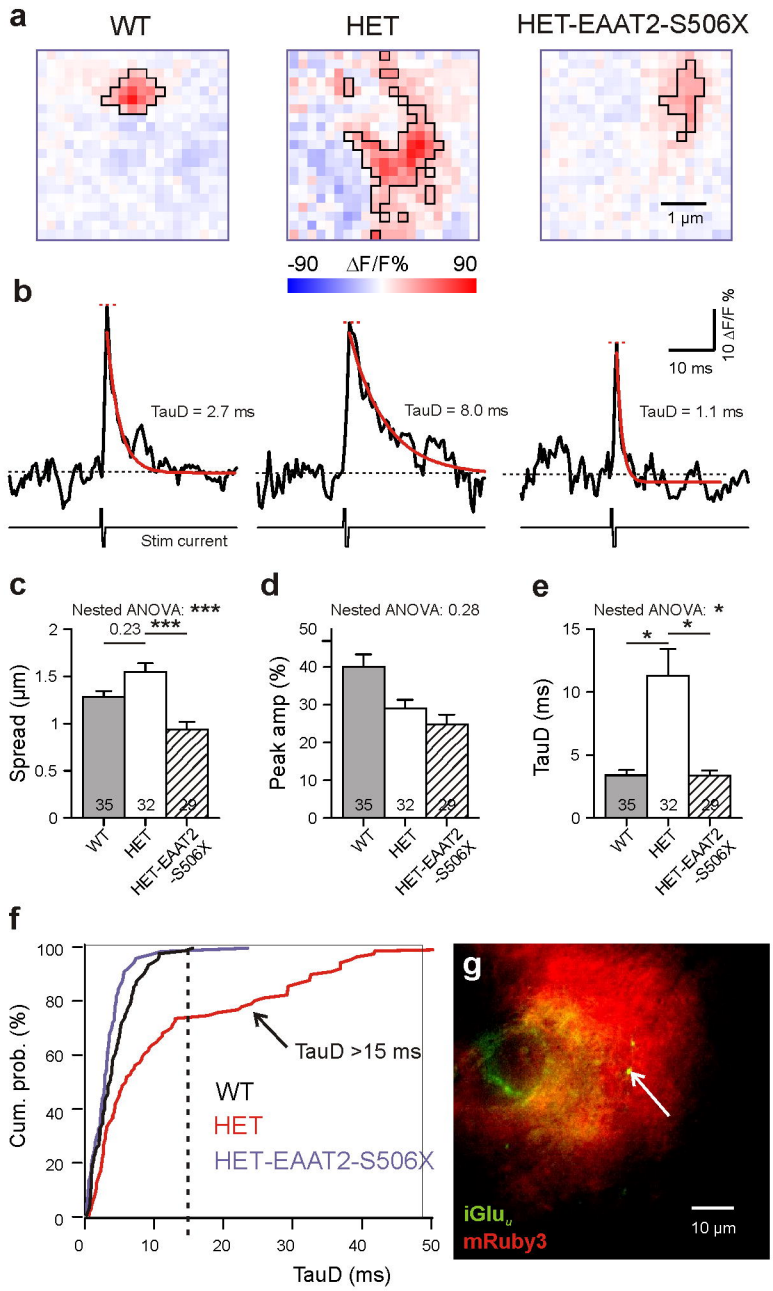

Fig. 6. Rescue of single synapse glutamate clearance in the striatum after expression of EAAT2-S506X. a *Specimens from single PT-type corticostriatal synaptic terminals in slices from WT, HET and treated HET. Bilateral intracranial injections of HET with EAAT2-S506X . The selected images were acquired at the response peak to illustrate the extension of iGlu$_u$ elevation (boxed area). Pink pixels within the black boundaries are pixels where stimulation of the bouton elicited a fluorescence increase (ΔF) to values larger than the resting level prior to stimulation (F).* ***b*** *Corresponding iGlu$_u$ values before and after electrical stimulation of the given bouton in the presence of TTX. The traces represent the mean value calculated from all suprathreshold pixels in the ROI. Red curves: Monoexponential functions fitted to the iGlu$_u$ traces. In black - respective time constants of decay (TauD).* ***c-e*** *Quantification of results.* ***f*** *Cumulative probability plot to illustrate the absence of TauD values >15 ms in WT and in EAAT2-S506X-treated HET. TauD values >15 ms identify pathological synapses in HET.* ***g*** *Only synapses in the immediate vicinity of transduced astrocytes were included, as confirmed by the location of the tested iGlu$_u$-expressing varicosity on the territory of mRuby3-positive astrocytes (arrowhead).*

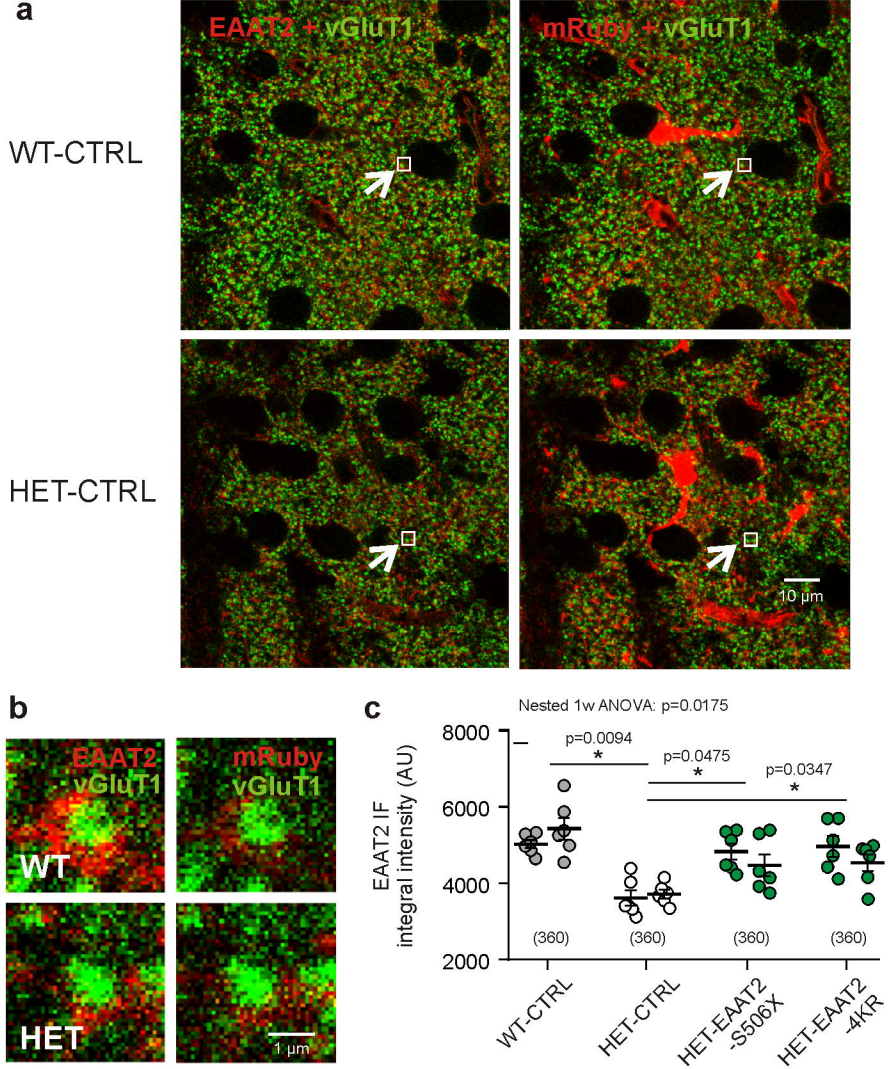

Fig. 7. Evaluation of synaptic EAAT2 immunofluorescence in fixed sections. ***a*** *Confocal images from WT-CTRL and HET-CTRL to illustrate the HD-related decrease in the overall EAAT2 IF. In the illustrated samples the mean intensity values were 3078 ± 38.4 (WT-CTRL) and 2673 ± 31.7 (HET-CTRL).* ***b*** *Regions of interest (ROIs) comprising just one synapse. The ROIs correspond to the small boxed areas in* ***a****. The EAAT2-immunopositive area corresponds to an astrocyte PAP, as it is labeled with mRuby3.* ***c*** *Quantification of integral EAAT2 IF from ROIs comprising only one vGluT1-immunopositive terminal. Numbers in brackets: evaluated synapses per group. Each data point is the mean value from 30 synapses on 1 mRuby3-labeled astrocyte. 12 astrocytes per group from 2 mice/group. Statistics: Nested data analysis.*

Supplemental Table 1. Summary of results.

HD phenotype	WT-CTRL				HET-CTRL				HET-S506X				Statistics			Posthoc MC HET-CTRL vs. HET-S506X		
	Mean	SE	N-c/t	N-a	Mean	SE	N-c/t	N-a	Mean	SE	N-c/t	N-a	Test	F (DFn, Dfd)	P	Test	P	Hedges' G
#CAG repeats	nd				186.1	1.2		22	185.6	1.7		15	t-test	t=0.24 (df=35)	ns			
Body weight at sacrifice	31.28	0.86		21	25.35	0.77		22	26.41	1.08		15	ANOVA	0.29 (2, 55)	<0.0001	Tukey	ns	
Step-over latency (s)	**56.7**	**10.00**		**18**	**179.1**	**46.6**		**19**	**51.6**	**9.8**		**14**	**Kruskal-Wallis**	**7.37 (2, 47)**	**0.0251**	**B-K-Y**	**0.041**	**0.79**
Open field #starts/stops (in 5 min)	**61.07**	**4.78**		**14**	**36.80**	**6.23**		**15**	**58.67**	**6.66**		**21**	**Kruskal-Wallis**	**4.17 (2, 47)**	**0.0216**	**B-K-Y**	**0.040**	**-0.78**
Mean running velocity (mm/s)	**99.53**	**5.14**		**14**	**81.57**	**6.04**		**15**	**109.45**	**8.06**		**21**	**ANOVA**	**4.15 (2, 26)**	**0.0220**	**Tukey**	**0.017**	**-0.87**
Mean velocity at rest (mm/s)	**37.39**	**1.78**		**14**	**26.48**	**3.69**		**15**	**36.91**	**3.12**		**21**	**ANOVA**	**3.72 (2, 47)**	**0.0318**	**Tukey**	**0.048**	**-0.70**
Open field total path (m/5 min)	**18.72**	**0.93**		**14**	**12.99**	**1.77**		**15**	**19.16**	**1.80**		**21**	**ANOVA**	**4.09 (2, 47)**	**0.0230**	**Tukey**	**0.027**	**-0.81**
Maximal/Mean rest radius	**2.53**	**0.04**		**14**	**2.81**	**0.11**		**15**	**2.58**	**0.21**		**21**	**ANOVA**	**4.64 (2, 47)**	**0.01**	**Tukey**	**0.038**	**0.75**
Open field center time (%)	**31.48**	**4.32**		**14**	**14.98**	**3.67**		**15**	**16.57**	**2.47**		**21**	**ANOVA**	**6.59 (2, 47)**	**0.0030**	Tukey	ns	
L-Asp-induced Na transient amp (ΔF/F%)*	**3.30**	**0.26**	**46**	**4**	**2.01**	**0.18**	**36**	**3**	**3.28**	**0.23**	**23**	**3**	**Nested ANOVA**	**4.525 (3 10)**	**0.0299**	**Dunnett**	**0.049**	**-1.0887**
Syn Glu transient(max) spread (µm)	**1.28**	**0.06**	**35**	**10**	**1.55**	**0.09**	**32**	**16**	**0.94**	**0.08**	**29**	**8**	**Nested ANOVA**	**10.90 (2, 31)**	**0.0003**	**B-K-Y**	**<0.001**	**1.27**
Syn Glu transient(max) TauD (ms)	**2.76**	**0.29**	**35**	**10**	**9.57**	**1.89**	**32**	**16**	**2.57**	**0.31**	**28**	**8**	**Nested ANOVA**	**5.04 (2, 31)**	**0.0127**	**B-K-Y**	**0.017**	**0.88**
Syn Glu transient(max) amp (ΔF/F%)	85.6	11.7	35	10	67.8	7.5	32	16	53.5	8.3	28	8	Nested ANOVA	0.76 (2,31)	0.4751	B-K-Y	ns	0.33
Syn EAAT2 IF total (a.u.)*	**5230**	**168.7**	**12/360**	**2**	**3663**	**81.42**	**12/360**	**2**	**4638**	**205.8**	**12/360**	**2**	**Nested ANOVA**	**12.25 (3,4)**	**0.0175**	**Dunnett**	**0.048**	**-1.87**
SPN input resistance (MOhm)	**114**	**10.3**	**18**	**8**	**165**	**17.0**	**14**	**8**	**127**	**13.5**	**8**	**5**	**Nested ANOVA**	**4.05 (2, 37)**	**0.0256**	B-K-Y	0.104	0.64
ITonic(GABA) amp (pA)	**11.33**	**2.37**	**13**	**6**	**2.99**	**1.03**	**14**	**8**	**5.78**	**3.37**	**7**	**5**	**Nested ANOVA**	**6.19 (2, 16)**	**0.0102**	B-K-Y	ns	

*Test includes 4KR group

Abbreviations: MC - multiple comparison test, BKY - Benjamini, Krieger, Yekutieli test